New atmospheric carbon isotopic measurements constrain the CO_2 rise during the last deglaciation

Anna Lourantou[1], Jošt V. Lavrič[1†], Peter Köhler[2], Jean-Marc Barnola[1+], Didier Paillard[3], Elisabeth Michel[3], Dominique Raynaud[1] and Jérôme Chappellaz[1*]

[1] Laboratoire de Glaciologie et Géophysique de l'Environnement (LGGE, CNRS, Université Joseph Fourier- Grenoble), St Martin d'Hères, France

[2] Alfred Wegener Institute for Polar and Marine Research, Bremerhaven, Germany

[3] Laboratoire des Sciences du Climat et de l'Environnement (IPSL/CEA, CNRS, Université Versailles-St Quentin), Gif-sur-Yvette, France

[†] Now at [3]

[+] Deceased

[*]Corresponding author: chappellaz@lgge.obs.ujf-grenoble.fr

Abstract

The causes of the ~80 ppmv increase of atmospheric carbon dioxide (CO_2) during the last glacial-interglacial climatic transition remain debated. We analyzed the parallel evolution of CO_2 and its stable carbon isotopic ratio ($\delta^{13}CO_2$) in the EPICA Dome C ice core to bring additional constraints. Agreeing well but largely improving the Taylor Dome ice core record of lower resolution, our $\delta^{13}CO_2$ record is characterized by a W-shape, with two negative $\delta^{13}CO_2$ excursions of 0.5‰ during Heinrich 1 and Younger Dryas events, bracketing a positive $\delta^{13}CO_2$ peak during the Bølling/Allerød warm period. The comparison with marine records and the outputs of two C-cycle box models suggests that changes in Southern Ocean

ventilation drove most of the CO_2 increase, with additional contributions from marine productivity changes on the initial CO_2 rise and $\delta^{13}CO_2$ decline and from rapid vegetation buildup during the CO_2 plateau of the Bølling/Allerød.

1. Introduction

Atmospheric CO_2 is the most important anthropogenic greenhouse gas and arguably the largest contributor to the current global warming [IPCC, 2007]. The monitoring of its stable carbon isotopic ratio ($\delta^{13}CO_2$) evolution is useful for the identification of biogeochemical processes driving the observed variations in CO_2. Former studies [Friedli et al., 1986; Francey et al., 1999] provided decisive evidence for the man-made origin of the CO_2 rise during the last 200 years, based on a ~1.5‰ decline of $\delta^{13}CO_2$ to its modern value of –7.8‰. This decrease is caused by the ^{13}C-depleted signature of the two major anthropogenic CO_2 sources, fossil fuel burning and carbon release from deforestation, having $\delta^{13}CO_2$ values of ~-30‰ and -25‰, respectively.

In contrast, natural changes in CO_2, such as the 80-ppmv rise over Termination I (hereafter TI), i.e. the transition from the Last Glacial Maximum (LGM ~20 ky BP, Before Present, the present being defined at 1950 Anno Domini AD; ky for kilo -10^3- years) to the Early Holocene (EH, ~10 ky BP), are still not well understood. Modeling studies attribute it to various oceanic processes, but without consensus on their relative importance [Broecker & Peng, 1986; Watson & Naveira Garabato, 2006]. Two major mechanisms in the ocean are usually invoked to explain the CO_2 glacial-interglacial (G-IG) changes: (i) a physical one, mainly related to Southern (S.) Ocean ventilation changes eventually releasing during Terminations old carbon stored in the deep ocean during the preceding glaciation [Toggweiler, 1999] and (ii) a biological one, involving the efficiency of nutrient utilization by phytoplankton in the Austral ocean, with decreased efficiency (and thus lower CO_2 uptake)

when atmospheric dust fertilization gets reduced [Archer et al., 2000; Sigman & Boyle, 2000]. For more than three decades scientists tried to disentangle the relative role of these or alternative processes, such as changes in oceanic pH and carbonate compensation [Archer et al., 2000], in the evolution of atmospheric CO_2. Currently, few models can reproduce the observed amplitude in G-IG CO_2 rise; they succeed only if all processes relevant on these time scales are considered [Köhler et al., 2005a; Brovkin et al., 2007].

To validate their hypothesis or to propose alternative ones, more observational constraints are needed. Paleo-atmospheric $\delta^{13}CO_2$ makes one of them and is central to our study. So far, a unique record of atmospheric $\delta^{13}CO_2$ through TI (including ~15 measurements) has been obtained from the Taylor Dome (TD) ice core [Smith et al., 1999 - SM1999 thereafter-], filling the time jigsaw between LGM and EH first produced from the Byrd core [Leuenberger et al., 1992]. Although of coarse resolution, the TD $\delta^{13}CO_2$ record has already been used to evaluate the output of several carbon (C) cycle models [Schulz et al., 2001; Brovkin et al., 2002; Köhler et al., 2005a; Obata, 2007]. For instance [Obata, 2007], using a coupled climate- C cycle model, simulates a decrease in net primary productivity and soil respiration during the Younger Dryas, in agreement with a combined increase of atmospheric CO_2 and minimum of $\delta^{13}CO_2$ observed in the TD ice core at that time. [Brovkin et al., 2002] emphasize the role of the G-IG reduced biological pump to explain the simultaneous CO_2 increase and $\delta^{13}CO_2$ decrease suggested by the TD data during the early part of the Termination.

In this study we: (1) present a new highly-resolved record of CO_2 and $\delta^{13}CO_2$ across TI from the EPICA Dome C (EDC) ice core, (2) compare it to existing ice core data (CO_2 from EDC [Monnin et al., 2001] and $\delta^{13}CO_2$ from TD [SM1999]), (3) propose a qualitative scenario on the causes of the deglacial CO_2 rise, based on a comparison with other proxies, and (4) test this scenario with two C-cycle box models [Köhler et al., 2005a; Paillard et al., 1993].

2. Method

A detailed description of the experimental method will be provided in [Lavrič et al., in prep.]. In short, 40-50 g of ice are cut in a cold room, removing about 3 mm of the original sample surface in order to avoid artefacts due to gas diffusion at the atmosphere/ ice interface [Bereiter et al., 2009]. The sample is then sealed in a stainless steel ball mill, evacuated and crushed to fine powder. The gas liberated from the bubbles is expanded over a -80°C ethanol/ liquid nitrogen (LN) water trap onto an evacuated 10 cm^3 sample loop. From there it is flushed by an ultra pure helium stream through a partially-heated glass trap where the CO_2 is frozen out at LN temperature (-196°C). The trapped CO_2 is then transferred into another ultra pure helium stream of lower flow rate, to be cryofocused on a small volume uncoated glass capillary tubing at LN temperature. The subsequent warming of the capillary allows the gas transfer with ultrapure helium into a gas chromatograph to separate the CO_2 from residual impurities (e.g. N_2O having the same mass over charge ratio as CO_2, [Ferretti et al., 2000]), its subsequent passage through an open split system to be finally directed to the isotope ratio mass spectrometer (IRMS, Finnigan MAT 252).

2.1. Signal determination and correction

2.1.1. Standard gases

The CO_2 mixing ratio in the ice samples is deduced from a linear regression between the varying pressure of several external standard gas injections and the corresponding CO_2 peak amplitude measured by the IRMS. The external standard gas has been prepared at CSIRO (Australia) and contains CO_2 = 260.3 ± 0.2 ppmv in dry air, with a $\delta^{13}CO_2$= –6.40±0.03‰ versus the international standard Vienna Pee-Dee Belemnite, VPDB ($\delta^{13}CO_2$ is reported in standard δ notation as the per mil (‰) difference between the stable carbon isotope composition of the sample and VPDB; $\delta^{13}C = [(^{13}C/^{12}C)_{sample} / (^{13}C/^{12}C)_{VPDB}] - 1$). It is pre-

concentrated and transferred throughout the system similarly as ice-core gas samples. Each sample or external standard introduction in the IRMS is bracketed with injections of a pure CO_2 standard reference gas (internal standard, ATMO MESSER, $\delta^{13}C$ = -6.5±0.1‰ versus VPDB) through another open split, to calibrate the IRMS and to correct for instrumental drift at the scale of a few minutes. Each spectrogram contains the sample/external standard peak, juxtaposed with peaks eluted from the internal standard gas. The mass over charge (m/z) 44 peak height of the internal standard injected with each gas sample is fitted as closely as possible to the expected CO_2 peak height from the ice-core gas sample or CSIRO standard, in order to avoid linearity corrections due to the IRMS response. The amount of the external standard gas processed before each ice-core gas sample expansion is also adjusted to the expected gas sample peak height for the same reason.

During the experimental protocol, the CSIRO external standard gas is processed seven times before, during and after the ice core gas sample measurement. The latter is usually processed several times, with three consecutive expansions of the same sample gas stored in the extraction container. Thus each data point corresponds to the average value of three replicate measurements of the same extracted gas. The pooled standard deviation on these replicates is 0.98 ppmv for CO_2 and 0.098‰ for $\delta^{13}CO_2$, while the pooled standard deviation on the routine daily processing of the CSIRO external standard gas is 0.90 ppmv for CO_2 and 0.15‰ for $\delta^{13}CO_2$. The last number does not directly translate to ice core measurements, as it integrates the large daily range of standard gas amount processed through the system and thus the non-linearity of the IRMS response, whereas each ice core gas sample is measured for $^{13}CO_2$ against a single standard gas peak having a comparable CO_2 amplitude.

On a daily basis, a correction is applied on the carbon isotopic ratios obtained on ice samples, based on the deviation observed between the external air standard measurements and the attributed CSIRO value. The correction relies on the seven external air standard injections

126 processed before the ice sample, in-between the three expansions of the ice sample, and after
127 the ice sample. On average, a systematic deviation of –0.30‰ from the attributed CSIRO
128 value was observed over the whole EDC measurement period, without any systematic trend
129 from day to day [Lavrič et al., in prep.].
130
131 **2.1.2. Blank tests**
132 Three different "blank tests" were conducted throughout the sampling period, with the
133 following differences compared with the procedure described above:
134 (I) No gas introduced in the sample loop. Results show a very low blank (residual
135 traces of CO_2 in the transfer lines and carrier gas): we obtain on average (n=35) a CO_2
136 amplitude equivalent to 0.33-1.7% of the external standard gas peak heights.
137 (II) A known quantity of external standard gas is introduced in an empty ice mill and
138 then processed to evaluate possible fractionations when expanding a known gas from the cold
139 mill to the sample loop.
140 (III) A known quantity of external standard gas is introduced in the ice mill together
141 with artificial bubble-free ice and then processed after crushing, to reproduce conditions
142 similar to those of a real ice core sample.
143 Results of the last two blank tests are shown in Table 1.
144 CO_2 results of the two blank tests are identical to the external standard gas value within
145 the analytical uncertainty (Table 1). The same applies for $\delta^{13}CO_2$ in test (II). On the other
146 hand, test (III) with bubble-free ice give an average $\delta^{13}CO_2$ depleted by ~0.3‰ compared to
147 the CSIRO value. This may arise from a small fractionation taking place when a gas sample
148 including a small amount of water vapour (vapour pressure at -60°C, i.e. the temperature in
149 the container) is transferred into the vacuum line. We decided not to apply such correction to
150 our measurements, due to insufficient statistics. The absolute values presented here should

151 thus be considered with caution, until we obtain good statistics on applying our system for
152 instance on numerous samples of pre-industrial and industrial ice. The $\delta^{13}CO_2$ signal for the
153 past 1000 y is well established [Francey et al., 1999]; numerical deviations obtained with our
154 system would confirm or infirm the need for such blank correction. If any, such small
155 possible bias does not affect the relative $\delta^{13}CO_2$ changes observed throughout Termination I.
156 Our results can thus safely be compared one to the other and discussed within the
157 experimental uncertainty range, being on average of 0.1‰.
158
159 **2.2. Corrections due to diffusion processes in the firn column**
160 Gas molecules in interstitial firn air mostly fractionate by molecular diffusion, in
161 addition to gravitational settling. The latter provokes a preferential accumulation of heavier
162 molecules (for the case of gases) or isotopologues (for the case of isotopes) at the bottom of
163 the firn column compared with the atmosphere [Craig et al., 1988; Schwander et al., 1993].
164 The fractionation is proportional to the mass difference between the involved gases; the one
165 between $^{13}CO_2$ and $^{12}CO_2$, is identical to ^{15}N versus ^{14}N of N_2. Therefore we use $\delta^{15}N$ of N_2
166 data from the EDC core, or modelled $\delta^{15}N$ of N_2 from an empirical relationship with δD in the
167 ice [both provided by G. Dreyfus, pers. communication] to correct $\delta^{13}CO_2$ for gravitational
168 fractionation. The CO_2 mixing ratio was also corrected for gravitational fractionation,
169 following [Etheridge et al., 1996].
170 Using measured or modelled $\delta^{15}N$ of N_2 changes the correction by a maximum of 0.03-
171 0.04‰. We finally used the modelled $\delta^{15}N$ of N_2, due to the limited depth coverage of the
172 measured $\delta^{15}N$ of N_2 data. For CO_2, the gravitational correction varies from -1.16 to -2.20
173 ppmv, while for $\delta^{13}CO_2$; it amounts between -0.41‰ (glacial ice) and -0.55‰ (Holocene ice).
174 Note that such correction was not applied to the previous EDC CO_2 record [Monnin et al.,
175 2001].

176 The difference of diffusion coefficient in air between $^{12}CO_2$ and $^{13}CO_2$ generates
177 changes in the $\delta^{13}CO_2$ signal in firn air and trapped bubbles due to molecular diffusion,
178 whenever CO_2 varies in the atmosphere, even when atmospheric $\delta^{13}CO_2$ remains unchanged.
179 The magnitude of this effect can be calculated with firn air diffusion models [Trudinger et al.,
180 1997]. Under present-day conditions when CO_2 increases by about 2 ppmv/y, the diffusion
181 correction on firn air and trapped bubbles composition amounts to about 0.10‰ on a 70-m
182 thick firn column [Trudinger et al., 1997]. Since the correction is at first order proportional to
183 the CO_2 rate of change, and as the largest observed CO_2 rate of change during TI is about 20
184 times smaller than the present-day increasing rate [Joos & Spahni, 2008], the molecular
185 diffusion correction would amount to less than 0.01‰ on the EDC $\delta^{13}CO_2$ profile, and is thus
186 neglected here.
187 A final possible correction on gas mixture measured in air bubbles is related to thermal
188 fractionation [Severinghaus et al., 2001; Grachev and Severinghaus, 2003]. As surface
189 temperature changes at EDC were too slow to generate large thermal gradients and gas
190 fractionation, and as no thermal anomaly was detected in the measured $\delta^{15}N$ of N_2 at EDC, no
191 thermal correction was applied to the measured $\delta^{13}CO_2$.
192
193 **2.3. Reliability of the record**
194 Greenland ice has been found to include in situ produced CO_2, involving either
195 carbonate/acid reaction or oxidation of organic compounds [Anklin et al., 1995; Tschumi &
196 Stauffer, 2000; Ahn et al., 2004]. No such artifact has been observed so far in Antarctic ice,
197 probably due to the much lower impurity content compared with Greenland ice.
198 All samples measured here originate from the EDC ice core drilled at Concordia Station
199 in Antarctica (75°06'S, 123°21'E; 3233m. above sea level) during the field season 1997-98.
200 Experimental or chemical artifacts affecting CO_2 and/or $\delta^{13}CO_2$ can be detected when the

scatter of duplicates exceeds 3σ of the external precision of the analytical technique. None of the investigated depth levels show such anomaly, thus indicating that the signal can be interpreted within the experimental uncertainty limits. On the other hand, one of the bag sections (dated at 12.6 ky in the EDC3_gas_a scale [Loulergue et al., 2007] cf. next section) provided reproducible mixing and isotopic ratios on duplicate measurements, but its average $\delta^{13}CO_2$ differed from neighboring bags (including trapped gas younger or older by less than 100 y) by more than 0.2‰. We hypothesize that the corresponding core section has been affected by anomalous storage and local transportation conditions (exposure to warm temperatures), leading to a suspicious result. We thus discard it in the following discussion.

2.4. Age scale

All EDC records are officially dated on the EDC3beta6 [Parrenin et al., 2007] and EDC3_gas_a [Loulergue et al., 2007] age scales for ice and gas data, respectively. However, in order to compare our EDC data with data from other cores (of marine or polar origin) and with model simulations constrained by other datasets, we synchronised both EDC and TD, using CH_4 as a time marker, to the newest Greenland chronology GICC05 [Rasmussen et al., 2006], using the Analyseries software [Paillard et al., 1996]. The tie-points for each core are presented in Table 2. The synchronised TD chronology is less constrained than the EDC one, due to the poorer time resolution of the TD CH_4 record [Köhler et al., 2005a]. The EDC ice chronology (for e.g. δD in Fig. 1a) is obtained by combining the CH_4 gas age fit on the GICC05 time scale and the Δage calculated with the EDC3beta6 chronology.

3. Results

Sixty three samples were measured from 50 different depth intervals (345 to 580 m of depth), covering the time period from 9 to 22 ky BP. This provides a mean time resolution of

220 y through the transition, whereas the previous published TD record offered a mean time resolution of only ~1000 y. Duplicate analyses of thirteen samples cut on the same ice bags yielded a reproducibility (1σ) of 0.99 ppmv and 0.1‰, respectively. The good correspondence between the reproducibility of CSIRO external standard measurements and of duplicate measurements of neighboring ice samples gives confidence in our main ice core signal structure. Measurements were performed exclusively on clathrate-free ice samples, at depths shallower than 600 m.

3.1. Comparison with previous datasets

The new CO_2 and $\delta^{13}CO_2$ datasets are plotted together with previously published data (CO_2, δD and CH_4) from EDC [Monnin et al., 2001; Jouzel et al., 2007; Loulergue et al., 2008] and TD [SM1999; Brook et al., 2000], as well as the $\delta^{18}O$ data from NGRIP core [NGRIP Members, 2004] in Fig. 1. The agreement between the detailed trends of both CO_2 records from the same EDC core [Monnin et al., 2001] is remarkable ($R^2 = 0.996$, Fig. 1d). Minor differences in the absolute values result from the use of different CO_2 international scales (SIO for the data of [Monnin et al., 2001], CSIRO in this study) and from the gravitational correction only applied to our dataset. The high temporal resolution allows the division of TI into four sub-periods (SP-I to SP-IV) as initiated by [Monnin et al., 2001], characterized by different rates of CO_2 change. With 40 measurements throughout TI, the data resolution is improved by more than a factor of two compared with SM1999 (Fig. 1d;e). Overall, the EDC and TD $\delta^{13}CO_2$ show similar mean values and trends in the course of TI, with 75% of the TD data falling within the 1σ EDC uncertainty (taking into account dating errors in the comparison). On the other hand, the TD CO_2 data are more scattered than the EDC ones.

Both EDC and TD $\delta^{13}CO_2$ records reveal a W-shape through TI, much more obvious in this new EDC record, with maximum amplitude of contiguous change of ~0.5‰, and a full $\delta^{13}CO_2$ range of 0.7‰. The better time resolution of the EDC profile reveals a more structured signal than the TD one within the ~0.1‰ experimental uncertainty, depicting notably faster transitions. This permits for the first time a detailed comparison of the isotopic signal with the changes in the CO_2 slope, within an uncertainty range comparable to the TD dataset (given as ±0.085‰ by SM1999). The latter value is probably a low estimate, as the atmospheric N_2O trend, needed to apply a correction on the TD $\delta^{13}CO_2$ measurements, was considered linear through the deglaciation, whereas the real N_2O signal reconstructed since shows a much different structure [Flückiger et al., 1999]. We remind that in our case no such N_2O correction is needed (cf. methods section).

3.2. CO_2 and $\delta^{13}CO_2$ trends throughout TI

Fig. 1d;e reveal a much different behavior between CO_2 and $\delta^{13}CO_2$: while CO_2 mostly shows linear trends within each sub-period (SP), $\delta^{13}CO_2$ exposes a more dynamic pattern during the SPs II to IV, with spikes and troughs superimposed on relatively stable boundary values.

LGM $\delta^{13}CO_2$ also shows a large variability whereas CO_2 bears little changes, a feature already observed with similar amplitude in previous datasets [Leuenberger et al., 1992; SM1999]. Part of the LGM $\delta^{13}CO_2$ variability parallels very small fluctuations in the CO_2 rate of change observed in the [Monnin et al., 2001] dataset. Between 22 and 17.6 ky BP, we obtain an average of 188±1 ppmv for CO_2 and –6.6±0.1‰ for $\delta^{13}CO_2$ (n=10).

The evolution of both CO_2 and $\delta^{13}CO_2$, with respect to Northern and Southern Hemisphere (hereafter NH and SH, respectively) climatic events, can be summarized as follows:

- Subsequent to the late LGM (22-17.6 ky BP), the early part of TI (SP-I, from 17.6 to 16.2 ky BP) is associated with a 25-ppmv rise of CO_2 and a 0.3‰ fall of $\delta^{13}CO_2$.

- SP-II (16.2 to 14.7 ky BP), during which the Heinrich 1 (H1) event ends in the NH (as deduced from ice-rafted debris in the N. Atlantic [Hemming, 2004] and also seen in NGRIP temperature data in Fig. 1b), reveals a two-step CO_2 rise; the first occurs until 15 ky with a progressive 14-ppmv increase and the second with a 12-ppmv rise within only 300 y. Meanwhile, $\delta^{13}CO_2$ experiences an oscillation of ~0.2‰ amplitude and reaches a minimum of –7.0±0.1‰ at about 15.5 ky BP, followed by a return to heavier values of ~ -6.8‰. A small $\delta^{13}CO_2$ peak also takes place at the start of SP-II, which coincides with a slightly smaller rate of CO_2 increase in the detailed Monnin et al. (2001) record. In a recent study, [Barker et al., 2009] introduced the notion of "Heinrich Stadial 1" to characterize oceanic conditions during the first two SP; we will refer to this notion in the following.

- SP-III (from 14.7 to 12.8 ky BP), coincident with the Antarctic Cold Reversal (ACR) in the SH and the Bølling/Allerød (B/A) warm event in the NH, is marked by a progressive 3-ppmv decrease of CO_2, while a positive excursion culminating at –6.5±0.1‰ during the mid-SP-III (~14.1 ky BP) is observed for $\delta^{13}CO_2$.

- SP-IV (between 12.8 and 11.6 ky BP), during which the Younger Dryas (YD) cold event in the NH and the post-ACR warming in the SH took place, reveals similar patterns for both CO_2 and $\delta^{13}CO_2$ as for SP-II. Thus, a progressive 13-ppmv CO_2 increase is observed until 12 ky, while a more abrupt rise of 10 ppmv is seen during the last 300 y. $\delta^{13}CO_2$ experiences a negative excursion of more than 0.2‰ amplitude, down to –7.0±0.1‰ (n=6).

- The EH (11.6 to 9 ky BP) $\delta^{13}CO_2$ mean level is more ^{13}C-enriched than during SP-IV and amounts to -6.8±0.1‰ (n=14). It also seems by 0.2±0.2‰ more depleted in ^{13}C than at the end of LGM. In contrast, previous studies concluded to more enriched $\delta^{13}CO_2$ values during the Holocene (by 0.16‰ in SM1999 to 0.2±0.2‰ [Leuenberger et al., 1992]) than at

300 the LGM. They were based on measurements performed on older LGM ice (Fig. 1d), while
301 Holocene data covered a different time window than considered here (from 9 to 7 ky BP,
302 GICC05 age scale, Fig. 1d;e). In addition, the Holocene $\delta^{13}CO_2$ level may be subject to
303 significant fluctuations, as pointed out by SM1999.

304 Our measurements show that, although $\delta^{13}CO_2$ starts to decrease in parallel with the
305 early CO_2 increase (a trend not captured in the less resolved SM1999 signal), its rapid drop
306 takes place ~1 ky later, when CO_2 has already increased by more than 10 ppmv. On the other
307 hand, the EH $\delta^{13}CO_2$ rise appears more modest in our dataset than in the TD record.
308

309 **4. Discussion**

310 Despite the small size of the $\delta^{13}CO_2$ signal to be deciphered and the relatively small
311 signal to noise ratio, some clear conclusions can now be drawn on its evolution during TI. Our
312 more detailed EDC $\delta^{13}CO_2$ signal compared to the TD one supports some of the earlier
313 conclusions drawn by SM1999. It also sheds some new light on the C-cycle dynamics during
314 the last deglaciation. The EDC record highlights an overall W-shape of atmospheric $\delta^{13}CO_2$
315 first broadly depicted by the SM1999 record throughout TI. It differs from SM1999 on the
316 following patterns:

317 1) the two well-resolved minima taking place at times of steadily and important rises of
318 CO_2 levels (late part of H1, and YD) reach comparable $\delta^{13}CO_2$ levels, around -7.0‰,

319 2) the CO_2 plateau accompanying the ACR goes together with a $\delta^{13}CO_2$ peak,

320 3) the average $\delta^{13}CO_2$ during the EH seems slightly more ^{13}C-depleted than at the end of
321 LGM,

322 4) SM1999 used a plot of $\delta^{13}CO_2$ as a function of the inverse of CO_2 (a so-called
323 "Keeling plot", i.e. a mixing diagram where the y-intercept should provide the isotopic
324 composition of the added CO_2 in the atmosphere), taking all T-I data together to discuss the

325 possible cause of the CO_2 increase. The improved time resolution of our dataset permits us to
326 sub-divide T-I with distinct intercepts through time. A y-intercept of -6‰ is obtained, similar
327 to all deglacial data of SM1999, but only through SP-II and SP-III data (not shown). On the
328 other hand, the two periods when CO_2 largely increases and $\delta^{13}CO_2$ simultaneously decreases
329 in our record (SP-I and SP-IV) reveal another "Keeling plot" type of isotopic signature for the
330 additional CO_2, similar for both sub-periods: ~-11‰ (Fig. 4). The main conclusion of
331 SM1999 that the C-cycle behaved in a dual mode depending on the speed of climatic changes
332 i.e. a slow mode taking place during the EH and LGM, and a fast mode during TI, is thus not
333 supported by the new Keeling plot (see supplementary material).
334 The similar "Keeling plot" signature of SP-I and SP-IV suggests at first hand that the
335 two main steps of atmospheric CO_2 increase during TI involved similar C-cycle mechanisms.
336 But their common y-intercept cannot be directly interpreted as the isotopic signature of such
337 mechanisms. Keeling plots work well only in an atmosphere-biosphere two-reservoir system
338 experiencing fast exchanges [e.g. Pataki et al., 2003]. On time scales of centuries to millennia
339 such as during TI, the isotopic buffering effect of the ocean (air/sea exchanges, carbonate
340 system) modifies the y-intercept in a three-reservoir model, as shown for instance by [Köhler
341 et al., 2006a] using the pre-industrial to industrial CO_2 increase and $\delta^{13}CO_2$ decrease as a case
342 study. Therefore, other approaches are required to extract possible scenarios out of our new
343 dataset, relevant to carbon exchanges between the atmosphere, ocean and biosphere during
344 TI. We use two of them here: a comparison with proxy records relevant to C-cycle processes,
345 and simulations of CO_2 and $\delta^{13}CO_2$ with two C-cycle box models.
346
347 **4.1. Comparison with other C-cycle proxy records**
348 The good correlation between CO_2 and Antarctic deuterium throughout TI (Fig. 1a;d),
349 already noticed in numerous works [e.g. Monnin et al., 2001; Bianchi and Gersonde, 2004],

350 points towards a leading role of the S. Ocean to drive the corresponding CO_2 evolution. As
351 pointed out in the introduction, two types of S. Ocean processes, a biological and a physical
352 one, can be evoked.

353 According to the first one, the S. Ocean during the LGM experienced a higher
354 productivity due to higher atmospheric dust fluxes bringing more iron, a limiting
355 micronutrient in high nutrient low chlorophyll (HNLC) regions [Martin, 1990]. As recorded
356 in e.g. EDC ice [Lambert et al., 2008; Gaspari et al., 2006] and shown in Fig. 2a, the
357 atmospheric dust (and iron) flux considerably decreases between ~18 and 14.6 ky BP,
358 corresponding to the first half of the CO_2 deglacial increase. This would imply a decreasing
359 biological pump in the S. Ocean exporting less carbon to the ocean interior and thus
360 increasing atmospheric CO_2. As phytoplankton preferentially assimilates the lighter carbon
361 isotope (^{12}C), a decreasing productivity would be accompanied by a decreasing atmospheric
362 $\delta^{13}CO_2$ [Brovkin et al., 2002], in agreement with our record. During the second half of TI, the
363 low dust values encountered in EDC ice suggest that the biologically-mediated mechanism in
364 the S. Ocean did not influence the CO_2 and $\delta^{13}CO_2$ trends.

365 The physical mechanism involves the rate of vertical mixing of the S. Ocean: the cold
366 LGM was associated with increased sea ice extent (mostly in winter) and with considerable
367 stratification of the S. Ocean water column [Sigman and Boyle, 2000; Stephens and Keeling,
368 2000; Marchitto et al., 2007]. The deep S. Ocean thus held a large amount of CO_2, due to
369 organic matter remineralization, with a strongly ^{13}C-depleted signature originating from
370 decomposed organic matter. [Duplessy et al., 1988] showed that changes in Atlantic
371 circulation at the end of LGM might have transferred low-$\delta^{13}C$ deep waters towards the ocean
372 surface, a phenomenon validated subsequently by [Curry and Oppo, 2005]. Overall, the
373 deglaciation, combining sea ice retreat, possible shifts of westerlies, and collapse of North
374 Atlantic Deep Water (NADW) formation during its early phase, would have generated a S.

375 Ocean stratification breakdown and hence, the release of deep ocean ^{13}C-depleted CO_2 in the
376 atmosphere, leading to an atmospheric CO_2 increase paralleled with a decrease of $\delta^{13}CO_2$ [e.g.
377 Toggweiler et al., 2006; Menviel et al., 2008]. Such mechanism could have also acted during
378 the YD, with a pause in-between during the B/A, when the NADW was probably switched on
379 again [Knorr and Lohmann, 2003]. As shown in Fig. 2, several proxy records, matching the
380 general shape of our $\delta^{13}CO_2$ record within their respective age model uncertainties, are in line
381 with this physical scenario:
382 1) During the Heinrich Stadial 1 and YD, NADW formation got weakened [Marchitto et
383 al., 1998], as evidenced by an increased $^{231}Pa/^{230}Th$ ratio in North Atlantic sediments (Fig. 2c)
384 [McManus et al., 2004]. This implies less NADW signal propagation towards the S. Ocean
385 waters.
386 2) NADW reduction is accompanied by a flushing of deep waters from the S. Ocean into
387 the Atlantic basin, thus equilibrating the water mass loss in the North Atlantic region. The
388 nutrient-enriched and ^{13}C-depleted signal of old Antarctic-dwelled waters (e.g. Antarctic
389 Intermediate Waters, AAIW) compared with deep waters from North Atlantic, is registered in
390 North Atlantic marine sediments through two negative $\delta^{13}C$-excursions during the Heinrich
391 Stadial 1 and YD [Rickaby & Elderfield, 2005] (Fig. 2d).
392 3) A high-resolution $\Delta^{14}C$ record from the North Pacific [Marchitto et al., 2007], shown
393 in Fig. 2e, reveals two negative excursions of more than 200‰ during the Heinrich Stadial 1
394 and the YD. They are interpreted as two episodes of transfer of old AAIW (including aged C
395 of up to 4-5 ky) into intermediate waters of the North Pacific, associated with the sea-ice
396 retreat [Stephens and Keeling, 2000] and the S. Ocean stratification breakdown [Marchitto et
397 al., 2007; Schmittner et al., 2007]. This should be accompanied by the release of sequestered
398 and ^{13}C-depleted deep oceanic carbon into the atmosphere. The scenario is corroborated at the
399 start of TI by a low resolution planktonic $\delta^{13}C$ record in subantarctic and equatorial Pacific

400 [Ninnemann and Charles, 1997; Spero and Lea, 2002]. A recent high-resolution tropical
401 Pacific planktic $\delta^{13}C$ record from [Stott et al., 2009], also reveals a nice W-trend throughout
402 the deglaciation, reinforcing the scenario of G-IG S. Ocean upwelling changes mentioned
403 above (Fig. 2f).

404 4) A high-resolution record of opal flux in the S. Ocean [Anderson et al., 2009], plotted
405 in Fig. 2g, shows an increase of upwelling strength in two steps, coincident with the Heinrich
406 Stadial 1 and YD, thus also pointing towards increased ventilation of deep S. Ocean waters as
407 a main trigger of the two steps in the deglacial CO_2 increase.

408 The physical mechanism involving S. Ocean stratification breakdown in two episodes
409 during TI thus qualitatively matches the CO_2 and $\delta^{13}CO_2$ trends, and could also explain the
410 common "Keeling plot" isotopic signature of the added carbon during the two episodes. Aside
411 from the biological pump and ocean circulation hypotheses, a possibly straightforward
412 explanation of the co-evolution between CO_2 and $\delta^{13}CO_2$ concerns changes in Sea Surface
413 Temperature (SST) during TI: due to isotopic fractionation during air/sea exchanges, a
414 warmer ocean will leave a ^{13}C-enriched signal in the atmosphere. SM1999 assigned a large
415 portion of their $\delta^{13}CO_2$ signal to this mechanism, by considering a globally averaged SST
416 increase of 5°C between the LGM and EH. On the other hand [Brovkin et al., 2002], using the
417 climate model CLIMBER-2, pointed out that the parallel changes of CO_2, alkalinity and
418 bicarbonate ion concentration significantly affect the isotopic fractionation during air/sea
419 exchanges, thus reducing the atmospheric $\delta^{13}CO_2$ imprint of SST changes. Moreover, the
420 rapid $\delta^{13}CO_2$ changes observed in our record may be difficult to reconcile with the speed of
421 SST changes in areas of deep water formation.

422 SP-III encounters terrestrial carbon buildup in vegetation, soils and peat deposits
423 [MacDonald et al., 2006] which could have contributed to the small CO_2 decrease and to a
424 positive $\delta^{13}CO_2$ anomaly in the atmosphere, as the biosphere preferentially assimilates ^{12}C.

425 This is qualitatively corroborated by the CH_4 evolution (Fig. 1c), pointing towards a switch-
426 on of boreal wetland CH_4 emissions (requiring a concomitant intensification of the terrestrial
427 C-cycle) at that time [Fischer et al., 2008]. Alternative scenarios attribute even more control
428 of the $\delta^{13}CO_2$ variability by terrestrial biosphere carbon uptake and release as a consequence
429 of abrupt temperature changes in the NH caused by the AMOC shutdown during H1 and YD
430 (e.g. Köhler et al., 2005b). For the deglacial CO_2 rise, the contribution from progressively
431 flooded continental shelves might also need some consideration [Montenegro et al., 2006];
432 however this scenario is challenged by the lag of the sea level increase with respect to CO_2
433 [Pépin et al., 2001

434 In summary, the qualitative comparison of the EDC CO_2 and $\delta^{13}CO_2$ records with C-
435 cycle proxies suggest a dominant role of increased overturning in the S. Ocean (as mainly
436 evidenced by $\Delta^{14}C$, opal flux and $\delta^{13}C$ records) during SP-I and SP-II to explain the two main
437 steps of CO_2 increase, with an additional contribution of reduced biological pump during SP-
438 I. The two mechanisms would have stalled during SP-III when NADW became stronger, and
439 would also have been counterbalanced by terrestrial carbon buildup. To go further into a
440 quantitative evaluation of mechanisms able to explain the CO_2 and $\delta^{13}CO_2$ signals, modeling
441 is required. In the following, we explore the problem using two C-cycle box models.
442

443 **4.2. BICYCLE model runs**

444 We employed the BICYCLE model [Köhler et al., 2005a], a coupled atmosphere/
445 ocean/ sediment/ biosphere C-cycle box model, run in a transient mode and forced with
446 various time-dependent paleoclimatic data over TI. It consists of a single atmospheric box
447 interacting with a 10-box ocean reservoir and the terrestrial biosphere, which is sub-divided
448 into 7 compartments [Köhler et al., 2005a]. The ocean further communicates with a sediment
449 reservoir. Mass balance equations are solved for the carbon stocks of the biospheric

450 compartments, for DIC, TAlk, PO_4 and O_2 in the 10 oceanic reservoirs, for CO_2 in the
451 atmosphere and for the carbon isotopes in all reservoirs.

452 BICYCLE is the only C-cycle model we are aware of which was run in transient mode
453 over TI. It was also used for the interpretation of atmospheric carbon records and deep ocean
454 $\delta^{13}C$ data over TI and much longer time scales of up to 2 My [Köhler et al., 2005a; Köhler et
455 al., 2006a; Köhler et al., 2006b; Köhler et al., 2006c; Köhler & Bintanja, 2008; Köhler et al.,
456 subm to Paleoceanography]. Since its application over TI [Köhler et al., 2005a],
457 improvements were performed in the parameterization of ocean circulation and sediment-
458 ocean interaction, we thus use new simulation results, instead of the model output published
459 in [Köhler et al., 2005a].

460

461 **4.2.1. Parameterizations**

462 The main model parameterizations, based on data obtained from ice core or marine
463 cores (Fig. 3) are the following:

464 1) Sea level rises by ~110m between 22 and 8 ky BP based on reconstructions of coral
465 reef terraces [Fairbanks, 1989] (Fig. 3A). This leads to changes in the salinity, in the
466 concentrations of all oceanic tracers and in the volumes of the oceanic boxes.

467 2) Temperature of all oceanic boxes is prescribed for present day from [Levitus & Boyer,
468 1994]. It changes over time according to oceanic proxy evidences for equatorial SST [Visser
469 et al., 2003] and deep ocean temperature [Labeyrie et al., 1987] (Fig. 3C). At high latitudes, it
470 is represented by ice core isotopic profiles (North Atlantic and North Pacific: $\delta^{18}O$ on
471 GICC05 age scale from NorthGRIP [NGRIP Members, 2004; Andersen et al., 2007], Fig. 3B;
472 S. Ocean: δD (corrected for the effect of sea level rise) from EDC [Parrenin et al., 2007;
473 Jouzel et al., 2001] synchronised to GICC05 [EPICA Community Members, 2006; Andersen

et al., 2007], as shown in Fig 3D. Both ice core records are scaled to provide a SST ΔT of 4 K between the minimum glacial values and the present-day.

3) Marine productivity in the S. Ocean is scaled (if allowed by macro-nutrient availability) on dust input to the S. Ocean as approximated by the non sea-salt-dust record measured in EDC [Roethlisberger et al., 2002] (Fig 3E).

4) Ocean circulation between the 10 boxes for present conditions is parameterized with data from the World Ocean Circulation Experiment WOCE [Ganachaud & Wunsch, 2000] (Fig 3F). Compared to the initial BICYCLE runs over TI [Köhler et al., 2005a], it was slightly modified to get a better agreement between simulated and reconstructed oceanic ^{13}C [Köhler et al., subm. to Paleoceanography]. About 30% of the upwelled waters in the S. Ocean are immediately redistributed to the intermediate equatorial Atlantic Ocean to account for the effect that, in the natural carbon cycle, upwelling waters in the S. Ocean (which are then flowing as water masses of intermediate depth to the north) are still enriched in DIC (Gruber et al., 2009).

Three major ocean currents are parameterized as follows (Fig. 3F):

- The strength of NADW (i.e. of its overturning, cf. [Köhler et al., 2005]) is assumed to be about 40% weaker [Meissner et al., 2003] during the LGM than at present day (10 versus 16 Sv), 2 Sv, 13 Sv and 11 Sv during the H1, B/A and YD, respectively [McManus et al., 2004].
- Antarctic-dwelled waters (e.g. Antarctic Bottom Waters, AABW), penetrating both the deep Atlantic (AABW_A) and deep Pacific (AABW_P), is strengthened when NADW weakens (i.e. during H1 and YD) and vice versa (for B/A), considering the north-south opposite trend during these abrupt climatic changes [Broecker, 1998; Rickaby & Elderfield, 2005; Kissel et al., 2008]. The EH and LGM AABW overall flux is set at of 15 Sv (6 SV for

498 the Atlantic branch and 9 Sv for the Pacific one). During H1 and YD (B/A), each section is
499 strengthened (weakened) by 3 Sv.
500 - Vertical mixing in the S. Ocean (SOX) is set to 0 Sv during LGM in accordance with
501 proxy evidence (e.g. $\delta^{13}C$ data from [Hodell et al., 2003; Spero & Lea, 2002]). Just after the
502 dust proxy (nss-Ca^{2+}) drop during SP-I, it is set to 15 Sv and maintained throughout B/A to be
503 finally increased by another 5 Sv at the end of YD [Köhler et al., 2005].
504 5) Changes in the terrestrial biosphere carbon pool are assumed to be primarily
505 temperature-dependent and made proportional to ¾ of the NorthGRIP $\delta^{18}O$ and ¼ of the EDC
506 δD changes (taken as temperature proxies), reflecting the latitudinal distribution of vegetated
507 land. The G-IG amplitude of land temperature change is considered as 8 K in the North and 5
508 K in the South. Net primary productivity is also parameterized on the modelled atmospheric
509 CO_2 values to take into account CO_2 fertilisation. More details on the terrestrial biosphere
510 module can be found in [Köhler & Fischer, 2004].
511 6) The additional effect of carbonate compensation [Archer & Maier-Reimer, 1994] to all
512 temporal changing processes listed above, is considered with a relaxation approach bringing
513 the deep ocean carbonate ion concentration back to initial values.
514 All ice core records (isotopic temperature proxies and nss-dust) are implemented as
515 500-y running means in the different parameterizations.
516
517 **4.2.2. BICYCLE model output**
518 The left panel of Fig. 5 illustrates the imprint Δ (with respect to the EH value) of major
519 processes simulated with BICYCLE, on atmospheric (a) CO_2 and (b) $\delta^{13}CO_2$. The reduction
520 of S. Ocean biological productivity (due to the onset of Fe-limitation in HNLC [Martin,
521 1990]), as well as the S. Ocean stratification breakdown [Spero & Lea, 2002] (associated with
522 sea-ice retreat and decreasing salinity [Watson & Naveira Garabato, 2006; Stephens &

523 Keeling, 2000]) are the main processes at work in the BICYCLE simulation at the TI
524 inception, provoking a 15 and 22-ppmv CO_2-rise and a 0.20 and 0.32 ‰ $\delta^{13}CO_2$ decline,
525 respectively.

526 During the NH cold events (H1 and YD), NADW weakens [McManus et al., 2004],
527 dampening the CO_2 increase and $\delta^{13}CO_2$ decrease related to AABW enhancement (+4.5
528 ppmv; -0.04‰) [Rickaby & Elderfield, 2005]; NADW (AABW) strengthening (weakening) at
529 the end of SP-II and SP-IV, combined with stronger S. Ocean water mixing at the end of YD,
530 lead to a CO_2 out-gassing of 10 and 7 ppmv, respectively (see supplementary material).

531 Sea level rise [Fairbanks, 1989] processes do not leave an important imprint on $\delta^{13}CO_2$
532 within the SPs, although they significantly affect CO_2 during the ACR, by provoking a 3-
533 ppmv reduction (see supplementary material). In contrast, vegetation growth, lagging S.
534 Ocean warming [Hughen et al., 2004] and forced by CO_2 fertilization and NH warming, starts
535 affecting $\delta^{13}CO_2$ during SP-II and becomes a major driver of this signal during SP-III and SP-
536 IV (green line of Fig. 5a;b). The rise-and-fall of total biospheric carbon by 200PgC during
537 SP-III and SP-IV respectively [Köhler & Fischer, 2004; Köhler et al., 2005a], lead to a 15-
538 ppmv decrease and a 17-ppmv rise of CO_2, also causing a +0.35‰ and -0.40‰ $\delta^{13}CO_2$
539 anomaly. This is in corroboration with previous numerical studies: for e.g. [Scholze et al.,
540 2003] assuming a total 180PgC decline of terrestrial carbon pools during YD, result in an
541 atmospheric CO_2 rise of 30 ppmv due to land cooling and precipitation decline, both
542 following the overturning circulation reduction. Köhler et al., 2005b find, as a consequence of
543 the AMOC shutdown and the accompanying northern hemispheric cooling, a total decline of
544 terrestrial carbon pools of up to 140 PgC, resulting in peak-to-peak changes in atmospheric
545 CO_2 and $\delta^{13}CO_2$ of 13 ppmv and 0.25‰, respectively. Recently, [Brovkin et al., 2007] used a
546 model of intermediate complexity to evaluate the shared contributions of different C-cycle
547 mechanisms on CO_2 and $\delta^{13}CO_2$ G-IG changes. They conclude to relative imprints of ocean

548 circulation, SST, land and marine productivity changes on $\delta^{13}CO_2$ very close to the BICYCLE
549 results.

550 **4.2.3. Data / model comparison**

551 The integrated signal from all the processes simulated with BICYCLE is compared with
552 our data in Fig. 5c for CO_2 and Fig. 5d for $\delta^{13}CO_2$. Throughout TI, BICYCLE produces an
553 increasing CO_2 trend, interrupted by phases of slower rate of increase or of stabilization, and
554 accompanied by a marked $\delta^{13}CO_2$ W-shaped trend. The lowest $\delta^{13}CO_2$ is simulated during
555 SP-II and SP-IV, with similar values around -7.0‰. A $\delta^{13}CO_2$ peak at the start of SP-III
556 reaches ~-6.5‰. BICYCLE thus captures the main features of the EDC records. A direct
557 comparison of Keeling plots, obtained with the data and the simulations is provided in Fig. 4.
558 Similar y-intercepts are obtained for the two main periods of abrupt CO_2 rise, suggesting that
559 the sequence and amplitude of the involved processes are well captured by the model
560 configuration. The Keeling plot comparison also highlights the limit of such plot, as the
561 similar y-intercepts generated by BICYCLE for the two periods come from a different
562 combination of C cycle mechanisms at work.

563 On the other hand, the timing of changes (for both CO_2 and $\delta^{13}CO_2$) can differ between
564 observations and model outputs. The EDC $\delta^{13}CO_2$ peak of SP-III and the minimum of SP-IV
565 appear earlier in the BICYCLE simulation. Both $\delta^{13}CO_2$ features mainly result from the
566 terrestrial component in BICYCLE, itself mainly parameterized on NH temperature. As both
567 EDC $\delta^{13}CO_2$ and the biosphere imprint in BICYCLE are on a common time scale (GICC05),
568 the shift cannot be attributed to dating errors. One explanation lies in the time response of
569 biospheric components to climate change being possibly underestimated in BICYCLE (a lag
570 of ~400y, also found by [Scholze et al., 2003]).

571 Another data/model difference appears during SP-IV, when BICYCLE simulates a CO_2
572 plateau and a large $\delta^{13}CO_2$ increase whereas the EDC data reveal a steady increase and a

573 minimum, respectively. Such BICYCLE output clearly depends on how well the timing and
574 amplitude of SST and ocean circulation changes are parameterized during the YD and EH. As
575 pointed out in the previous section, C-cycle proxy data suggest that the S. Ocean mixing
576 should have driven the YD CO_2 increase (it is parameterized as constant in the model),
577 whereas the BICYCLE simulation gives more weight to terrestrial carbon release and SST
578 increase.

579 The box model bears other uncertainties and potential biases, such as: (i) the relative
580 dating of the various input signals and their synchronization with ice cores, (ii) the pertinence
581 of the proxies used for each process (e.g. the magnitude of oceanic fluxes throughout TI), (iii)
582 the coarse spatial resolution of low-latitudes. Still, it shows that the general shape of the EDC
583 CO_2 and $\delta^{13}CO_2$ signals can be reproduced with a reasonable temporal sequence of C-cycle
584 mechanisms. It supports a scenario where S. Ocean stratification breakdown and decrease of
585 marine productivity jointly explain the early half of the CO_2 and $\delta^{13}CO_2$ signals, with the
586 terrestrial biosphere intervening in the shape of both signals during the B/A. The conclusion
587 to be drawn for the YD episode is less clear, as the box model produces a $\delta^{13}CO_2$ minimum
588 but fails to simulate the parallel CO_2 increase.

589 A crucial point when comparing temporally highly-resolved atmospheric records
590 derived from ice cores with transient model simulations is that the gas records are smoothed
591 by gas diffusion in the firn and by progressive bubble close-off. Therefore, they do not
592 represent one single point in time, but are averaged over decades to centuries, mainly
593 depending on accumulation rate and temperature. A gas diffusion and enclosure model
594 [Spahni et al., 2003] was used earlier to calculate the age distribution for CO_2 in EDC and the
595 attenuation of atmospheric signals during the enclosure process. It has been calculated that the
596 gas records represent averages between 213 (preindustrial) and 590 (LGM) y with a
597 lognormal-shapelike age distribution [Joos and Spahni, 2008]. As a consequence, BICYCLE

598 model simulations, which should represent atmospheric records before gas enclosure, might
599 not be directly comparable with ice core records, especially for low accumulation sites and
600 fast processes, because original atmospheric amplitudes are attenuated during the enclosure
601 process [Köhler et al, submitted]. A solution would be to proceed to similar measurements for
602 the same time interval on a core with larger accumulation rate.
603
604 **4.3. BOXKIT model**
605 We also applied BOXKIT, a conceptual ocean/atmosphere model run under equilibrium
606 states [Paillard et al., 1993]. The ocean is splitted in 10 boxes, 5 for the surface, 2 for
607 intermediate waters and 3 for the deep ocean. BOXKIT includes a single atmospheric box, but
608 no terrestrial biosphere. The same forcings as BICYCLE are applied for 6 'snapshots' over
609 TI.
610 Similar overall trends as those of BICYCLE, both for CO_2 and $\delta^{13}CO_2$ are obtained (red
611 squares in Fig. 5c;d). As BOXKIT provides easier tuning than BICYCLE to carry on
612 sensitivity tests, we used it to evaluate the output sensitivity to low latitudes SST. Increasing
613 tropical SSTs by 3°C (instead of 0.5°C as done for BICYCLE forcings) for the SP-III
614 simulation, concomitantly with NH warming as is seen in N. Atlantic sediment data from e.g.
615 [Lea et al., 2003], leads to a $\delta^{13}CO_2$ increase by ~0.2‰, more in line with the EDC data. This
616 example shows the non-uniqueness of solutions when interpreting the C-cycle data with box
617 models.
618
619 **5. Conclusions**
620 Our new record of $\delta^{13}CO_2$ from the EDC ice core over the last deglaciation reveals
621 sharp fluctuations mostly associated with variations in the CO_2 rate of change. A comparison
622 with other CO_2 and $\delta^{13}CO_2$ ice core data gives confidence in the validity of this new dataset.

623 In addition, consistent standard deviations are observed between different statistical
624 approaches of the experimental system. The general shape of the deglacial $\delta^{13}CO_2$ signal can
625 be summarized as a "W", with two minima accompanying the two major steps of CO_2
626 increase, and a peak when CO_2 gets stabilized or slightly decreasing.

627 The comparison with C-cycle related proxies highlights similarities with marine signals
628 associated with the strength of S. Ocean ventilation and upwelling, suggesting that this
629 physical mechanism would be the main driver of the deglacial CO_2 increase.

630 Two C-cycle box models (BICYCLE and BOXKIT), run under the same input
631 parameters support the dominant role of S. Ocean physical processes and add the marine
632 productivity decline during the early part of the deglaciation as another mechanism
633 contributing to the $\delta^{13}CO_2$ decrease and CO_2 increase. The BICYCLE model supports an
634 additional role of terrestrial carbon buildup to explain the CO_2 plateau and $\delta^{13}CO_2$ peak
635 paralleling the ACR. It also simulates an early YD $\delta^{13}CO_2$ minimum followed by an increase
636 to EH values, attributed to terrestrial carbon and SST decrease and subsequent increase, an
637 explanation conflicting with C-cycle proxy data which suggest a dominant role of
638 strengthening S. Ocean ventilation. The failure of BICYCLE to simulate a parallel CO_2
639 increase shows the limit of this modeling exercise, which crucially depends on assumptions
640 regarding SO upwelling changes.

641 More sophisticated approaches using coupled carbon-climate Earth system models will
642 be needed in the future to better disentangle the contribution of each process, with their direct
643 parameterizations in the models instead of the use of proxies. Our detailed EDC profile
644 clearly highlights the need for fine time resolution in producing future $\delta^{13}CO_2$ records
645 throughout major climatic events.

646

647

Acknowledgments

This work is a contribution to the European Project for Ice Coring in Antarctica (EPICA), a joint ESF (European Science Foundation)/ EC scientific program, funded by the European Commission and by national contributions from Belgium, Denmark, France, Germany, Italy, the Netherlands, Norway, Sweden, Switzerland and the United Kingdom. The main logistic support was provided by IPEV and PNRA (at Dome C). AL was funded by the European Research Training and Mobility Network GREENCYCLES. Additional funding support was provided by the QUEST-INSU project DESIRE, the FP6 STREP EPICA-MIS, and the French ANR PICC (ANR-05-BLAN-0312-01). Long-term support for the mass spectrometry work at LGGE was provided by the Fondation de France and the Balzan Price. Discussions with G. Dreyfus, H. Schaefer and G. Delaygue were very much appreciated. We particularly thank C. Lorius for his confidence in our earlier work and five anonymous reviewers for fruitful comments on previous versions of this manuscript. This is EPICA publication no XXX.

Reference list

Ahn J., Wahlen M., Deck B. L., Brook E. J., Mayewski P. A., Taylor K. C. and White J. W. C. (2004): A record of atmospheric CO_2 during the last 40,000 years from the Siple Dome, Antarctica ice core. *Journal of Geophysical Research* 109, D13305, DOI: 10.1029/2003JD004415.

Andersen K. K., Svensson A., Johnsen S. J., Rasmussen S. O., Bigler M., Röthlisberger R., Ruth U., Siggaard-Andersen M.-L., Steffensen J. P., Dahl-Jensen D., Vinther B. M. and Clausen H. B. (2007): The Greenland Ice Core Chronology 2005, 15–42 ka. Part 1: constructing the time scale. *Quaternary Science Reviews* 25(23-24), pp. 3246-3257.

672 Anderson R. F., Ali S., Bradtmiller L. I., Nielsen S. H. H., Fleisher M. Q., Anderson B. E. and
673 Burckle L. H. (2009): Wind-driven upwelling in the Southern Ocean and the deglacial rise in
674 atmospheric CO_2. *Science* 323(5920), pp. 1443-1448.
675 Anklin M., Barnola J.-M., Schwander J., Stauffer B. and Raynaud D. (1995): Processes
676 affecting the CO_2 concentrations measured in Greenland ice. *Tellus* 47B, pp. 461-470.
677 Archer D., and E. Maier-Reimer (1994): Effect of deep-sea sedimentary calcite preservation
678 on atmospheric CO_2 concentration. *Nature* 367(6460), pp. 260 - 263.
679 Archer D., Winguth A., Lea D. and Mahowald N. (2000): What caused the glacial/interglacial
680 atmospheric pCO_2 cycles? *Reviews of Geophysics* 38(2), pp. 159-190.
681 Barker S., Diz P., Vautravers M. J., Pike J., Knorr G., Hall I. R. and Broecker W. S. (2009):
682 Interhemispheric Atlantic seesaw response during the last deglaciation. *Nature* 457(7233), pp.
683 1097-1102.
684 Bereiter B., Schwander J., Lüthi D. and Stocker T. F. (2009): Change in CO_2 concentration
685 and O_2/N_2 ratio in ice cores due to molecular diffusion *Geophysical Research Letters* 36,
686 L05703, DOI: 10.1029/2008GL036737.
687 Bianchi C., and R. Gersonde (2004): Climate evolution at the last deglaciation: the role of the
688 Southern Ocean. *Earth and Planetary Science Letters*, 228(3-4), pp. 407-424.
689 Broecker W. S., and T. H. Peng (1986): Carbon cycle: 1985 glacial to interglacial changes in
690 the operation of the global carbon cycle. *Radiocarbon*, 28(2A), pp. 309-327.
691 Broecker W. S. (1998): Paleocean circulation during the last deglaciation: A bipolar seesaw?
692 *Paleoceanography* 13(2), pp. 119-121.
693 Brook E. J., Harder S., Severinghaus J., Steig E. J. and Sucher C. M. (2000): On the origin
694 and timing of rapid changes in atmospheric methane during the last glacial period. *Global*
695 *Biogeochemical Cycles* 14(2), pp. 559–572.

696 Brovkin V., Hofmann M., Bendtsen J. and Ganopolski A. (2002): Ocean biology could
697 control atmospheric $\delta^{13}C$ during glacial-interglacial cycle. *Geochem., Geophys., Geosyst.*
698 3(5), DOI: 10.1029/2001GC000270.
699 Brovkin V., Ganopolski A., Archer D. and Rahmstorf S. (2007): Lowering of glacial
700 atmospheric CO_2 in response to changes in oceanic circulation and marine biogeochemistry.
701 *Paleoceanography* 22, PA4202, DOI: 10.1029/2006PA001380.
702 Craig H., Horibe Y. and Sowers T. (1988): Gravitational separation of gases and isotopes in
703 polar ice caps. *Science* 242(4886), pp. 1675 - 1678.
704 Curry W. B. and Oppo D. W. (2005): Glacial water mass geometry and the distribution of
705 $\delta^{13}C$ of ΣCO_2 in the western Atlantic Ocean. *Paleoceanography* 20, PA1017, DOI:
706 10.1029/2004PA001021.
707 Duplessy J. C., Shackleton N. J., Fairbanks R. G., Labeyrie L., Oppo D. and Kallel N. (1988):
708 Deepwater source variations during the last climatic cycle and their impact on the global
709 deepwater circulation. *Paleoceanography* 3(3), pp. 343-360.
710 EPICA Community Members (2006): One-to-one coupling of glacial climate variability in
711 Greenland and Antarctica. *Nature*, 444(7116), pp. 195-198.
712 Etheridge D. M., Steele L. P., Langenfelds R. L., Francey R. J., Barnola J.-M. and Morgan V.
713 I. (1996): Natural and anthropogenic changes in atmospheric CO_2 over the last 1000 years
714 from air in Antarctic ice and firn. *Journal of Geophysical Research* 101(D2), pp. 4115–4128.
715 Fairbanks R. G. (1989): A 17,000-year glacio-eustatic sea level record: influence of glacial
716 melting rates on the Younger Dryas event and deep-ocean circulation. *Nature*, 342(6250), pp.
717 637 – 642.
718 Ferretti D. F., Lowe D. C., Martin R. J. and Brailsford G. W. (2000): A new gas
719 chromatograph-isotope ratio mass spectrometry technique for high-precision, N_2O-free

720 analysis of $\delta^{13}C$ and $\delta^{18}O$ in atmospheric CO_2 from small air samples. *Journal of Geophysical*
721 *Research* 105(D5), pp. 6709-6718.
722 Fischer H., Behrens M., Bock M., Richter U., Schmitt J., Loulergue L., Chappellaz J., Spahni
723 R., Blunier T., Leuenberger M. and Stocker T. F. (2008): Changing boreal methane sources
724 and constant biomass burning during the last termination. *Nature* 452(7189), pp. 864-867.
725 Flückiger J., Dällenbach A., Blunier T., Stauffer B., Stocker T. F., Raynaud D. and Barnola
726 J.-M. (1999): Variations in atmospheric N_2O concentration during abrupt climatic changes.
727 *Science* 285(5425), pp. 227-230.
728 Francey R. J., Allison C. E., Etheridge D. M., Trudinger C. M., Enting I. G., Leuenberger M.,
729 Langenfelds R. L., Michel E. and Steele L. P. (1999): A 1000-year high precision record of
730 $\delta^{13}C$ in atmospheric CO_2. *Tellus B* 51(2), pp. 170–193.
731 Friedli H., Lötscher H., Oeschger H., Siegenthaler U. and Stauffer B. (1986): Ice core record
732 of the $^{13}C/^{12}C$ ratio of atmospheric CO_2 in the past two centuries. *Nature* 324(6094), pp. 237-
733 238.
734 Ganachaud A. and Wunsch C. (2000): Improved estimates of global ocean circulation, heat
735 transport and mixing from hydrographic data. *Nature* 408(6811), pp. 453-457.
736 Gaspari V., Barbante C., Cozzi G., Cescon P., Boutron C. F., Gabrielli P., Capodaglio G.,
737 Ferrari C., Petit J. R. and Delmonte B. (2006): Atmospheric iron fluxes over the last
738 deglaciation: Climatic implications. *Geophysical Research Letters* 33, L03704, DOI:
739 10.1029/2005GL024352.
740 Grachev A. M. and Severinghaus J. P. (2003): Laboratory determination of thermal diffusion
741 constants for $^{29}N_2/^{28}N_2$ in air at temperatures from −60 to 0 °C for reconstruction of
742 magnitudes of abrupt climate changes using the ice core fossil–air paleothermometer.
743 *Geochimica et Cosmochimica Acta* 67(3), pp. 345-360.

744 Gruber N., Gloor M., Mikaloff Fletcher S. E., Doney S. C., Dutkiewich S., Follows M. J.,
745 Gerber M., Jacobson A. R., Joos F., Lindsay K., Menemenlis D., Mouchet A., Müller S. A.,
746 Sarmiento J. L., Takahashi T. (2009): Oceanic sources, sinks and transport of atmospheric
747 CO_2. Global Biogeochemical Cycles 23, GB1005, DOI: 10.1029/2008GB003349.
748 Hemming S. R. (2004): Heinrich events: Massive late Pleistocene detritus layers of the North
749 Atlantic and their global climate imprint. *Reviews of Geophysics* 42, RG1005, DOI:
750 10.1029/2003RG000128.
751 Hodell D. A., Venz K. A., Charles C. D. and Ninnemann U. S. (2003): Pleistocene vertical
752 carbon isotope and carbonate gradients in the South Atlantic sector of the Southern Ocean.
753 *Geochemistry, Geophysics, Geosystems* 4(1), CiteID 1004, DOI: 10.1029/2002GC000367.
754 Hughen K. A., Eglinton T. I., Xu L. and Makou M. (2004): Abrupt tropical vegetation
755 response to rapid climate changes. *Science* 304(5679), pp. 1955-1959.
756 IPCC (2007): Climate Change 2007: The Physical Science Basis. Contribution of Working
757 Group I to the Fourth Assessment Report of the Intergovernmental Panel on Climate Change
758 [Solomon, S., D. Qin, M. Manning, Z. Chen, M. Marquis, K.B. Averyt, M. Tignor and H.L.
759 Miller (eds.)]. *Cambridge University Press*, Cambridge, United Kingdom and New York, NY,
760 USA, 996 pp.
761 Joos F. and Spahni R. (2008): Rates of change in natural and anthropogenic radiative forcing
762 over the past 20,000 years. *PNAS* 105(5), pp. 1425-1430.
763 Jouzel J., Masson V., Cattani O., Falourd S., Stievenard M., Stenni B., Longinelli A., Johnsen
764 S. J., Steffenssen J. P., Petit J. R., Schwander J., Souchez R. and Barkov N. I. (2001): A New
765 27 Ky high resolution east Antarctic climate record. *Geophysical Research Letters* 28(16), pp.
766 3199-3202.
767 Jouzel J., Masson-Delmotte V., Cattani O., Dreyfus G., Falourd S., Hoffmann G., Minster B.,
768 Nouet J., Barnola J. M., Chappellaz J., Fischer H., Gallet J. C., Johnsen S., Leuenberger M.,

769 Loulergue L., Luethi D., Oerter H., Parrenin F., Raisbeck G., Raynaud D., Schilt A.,
770 Schwander J., Selmo E., Souchez R., Spahni R., Stauffer B., Steffensen J. P., Stenni B.,
771 Stocker T. F., Tison J. L., Werner M. and Wolff E. W. (2007): Orbital and Millennial
772 Antarctic Climate Variability over the Past 800,000 Years. *Science* 317(5839), pp. 793 - 796.
773 Kissel C., Laj C., Piotrowski A. M., Goldstein S. L. and Hemming S. R. (2008): Millennial-
774 scale propagation of Atlantic deep waters to the glacial Southern Ocean. *Paleoceanography*
775 23, PA2102, DOI: 10.1029/2008PA001624.
776 Knorr G. and Lohmann, G. (2003): Southern Ocean Origin for Resumption of Atlantic
777 Thermohaline Circulation during Deglaciation, *Nature* 424, pp. 532-536.
778 Köhler P. and Fischer H. (2004): Simulating changes in the terrestrial biosphere during the
779 last glacial/interglacial transition. *Global and Planetary Change* 43(1-2), pp. 33-55.
780 Köhler P., Fischer H., Munhoven G. and Zeebe R. E. (2005a): Quantitative interpretation of
781 atmospheric carbon records over the last glacial termination. *Global Biogeochemical Cycles*
782 19, GB4020, DOI: 10.1029/2004GB002345.
783 Köhler P., Joos, F., Gerber, S., Knutti, R.(2005b): Simulated changes in vegetation
784 distribution, land carbon storage, and atmospheric CO_2 in response to a collapse of the North
785 Atlantic thermohaline circulation, *Climate Dynamics*, 25, pp. 689-708, DOI:10.1007/s00382-
786 005-0058-8.
787 Köhler P., Fischer H., Schmitt J. and Munhoven G. (2006a): On the application and
788 interpretation of Keeling plots in paleo climate research – deciphering $\delta^{13}C$ of atmospheric
789 CO_2 measured in ice cores. *Biogeosciences* 3, pp. 539-556.
790 Köhler P., Muscheler R. and Fischer H. (2006b): A model-based interpretation of low-
791 frequency changes in the carbon cycle during the last 120,000 years and its implications for
792 the reconstruction of atmospheric $\Delta^{14}C$. *Geochemistry Geophysics Geosystems* 7, Q11N06,
793 DOI: 10.1029/2005GC001228.

794 Köhler P. and Fischer H. (2006c): Simulating low frequency changes in atmospheric CO_2
795 during the last 740,000 years. *Climate of the Past* 2(2), pp. 57-78.
796 Köhler P. and Bintanja R. (2008): The carbon cycle during the Mid Pleistocene transition: the
797 Southern Ocean decoupling hypothesis. *Clim. Past* 4, pp. 311-332.
798 Köhler P., Fischer H. and Schmitt J. (submitted): Atmospheric $\delta^{13}CO_2$ and its relation to
799 pCO_2 and deep ocean $\delta^{13}C$ during the last Pleistocene. *Paleoceanography,* DOI:
800 10.1029/2008PA001703.
801 Labeyrie L. D., Duplessy J. C. and Blanc P. L. (1987): Variations in mode of formation and
802 temperature of oceanic deep waters over the past 125,000 years. *Nature* 327(6122), pp. 477-
803 482.
804 Lambert F., Delmonte B., Petit J. R., Bigler M., Kaufmann P. R., Hutterli M. A., Stocker T.
805 F., Ruth U., Steffensen J. P. and Maggi V. (2008): Dust-climate couplings over the past
806 800,000 years from the EPICA Dome C ice core. *Nature* 452(7187), pp. 616-619.
807 Lavrič J. V., Lourantou A., Barnola J.-M., Michel E., Raynaud D. and Chappellaz J (in prep.):
808 Measurement of carbon isotope composition and mixing ratio of CO_2 in ancient air from ice
809 core samples.
810 Lea D. W., Pak D. K., Peterson L. C. and Hughen K. A. (2003): Synchroneity of tropical and
811 high-latitude Atlantic temperatures over the last glacial Termination. *Science* 301(5638), pp.
812 1361 - 1364.
813 Leuenberger M., Siegenthaler U. and Langway C. C. (1992): Carbon isotope composition of
814 atmospheric CO_2 during the last ice age from an Antarctic ice core. *Nature* 357(6378), pp.
815 488-490.
816 Levitus and Boyer. (1994): *World Ocean Atlas* Vol 4: Temperature.

817 Loulergue L., Parrenin F., Blunier T., Barnola J.-M., Spahni R., Schilt A., Raisbeck G. and
818 Chappellaz J. (2007): New constraints on the gas age-ice age difference along the EPICA ice
819 cores, 0–50 kyr. *Clim. Past* 3(3), pp. 527-540.
820 Loulergue L., Schilt A., Spahni R., Masson-Delmotte V., Blunier T., Lemieux B., Barnola J.-
821 M., Raynaud D., Stocker T. F. and Chappellaz J. (2008): Orbital and millennial-scale features
822 of atmospheric CH_4 over the past 800,000 years. *Nature* 453(7193), pp. 383-386.
823 MacDonald G. M., Beilman D. W., Kremenetski K. V., Sheng Y., Smith L. C. and Velichko
824 A. A. (2006): Rapid early development of circumarctic peatlands and atmospheric CH_4 and
825 CO_2 variations. *Science* 314(5797), pp. 285-288.
826 Marchitto J. T. M., Curry W. B. and Oppo D. W. (1998): Millennial-scale changes in North
827 Atlantic circulation since the last Glaciation. *Nature* 393(6685), pp. 557-561.
828 Marchitto T. M., Lehman S. J., Ortiz J. D., Flückiger J. and Geen A. v. (2007): Marine
829 radiocarbon evidence for the mechanism of deglacial atmospheric CO_2 rise. *Science*
830 316(5830), pp. 1456 - 1459.
831 Martin J. H. (1990): Glacial-Interglacial CO_2 Change: The iron hypothesis *Paleoceanography*
832 5(1), 1-13.
833 McManus J. F., Francois R., Gherardi J.-M., Keigwin L. D. and Brown-Leger S. (2004):
834 Collapse and rapid resumption of Atlantic meridional circulation linked to deglacial climate
835 changes. *Nature* 428(6985), pp. 834-837.
836 Meissner K. J., Schmittner A., Weaver A. J. and Adkins J. F. (2003): Ventilation of the North
837 Atlantic Ocean during the Last Glacial Maximum: A comparison between simulated and
838 observed radiocarbon ages. *Paleoceanography* 18(2), ID1023, DOI: 10.1029/2002PA000762.
839 Menviel L., Timmermann A., Mouchet A. and Timm O. (2008): Climate and marine carbon
840 cycle response to changes in the strength of the Southern Hemispheric westerlies.
841 *Paleoceanography* 23, PA4201, DOI: 10.1029/2008PA001604.

842 Monnin E., Indermühle A., Dällenbach A., Flückiger J., Stauffer B., Stocker T. F., Raynaud
843 D. and Barnola J.-M. (2001): Atmospheric CO_2 concentrations over the last glacial
844 Termination. *Science* 291(5501), pp. 112 - 114.
845 Montenegro A., Eby M., Kaplan J. O., Meissner K. J. and Weaver A. J. (2006): Carbon
846 storage on exposed continental shelves during the glacial-interglacial transition. *Geophysical*
847 *Research Letters* 33, L08703, DOI: 10.1029/2005GL025480.
848 NGRIP Members (2004): High-resolution record of Northern Hemisphere climate extending
849 into the last interglacial period. *Nature* 431(7005), pp. 147-151.
850 Ninnemann U. S. and Charles C. D. (1997): Regional differences in Quaternary subantarctic
851 nutrient cycling: link to intermediate and deep water ventilation. *Paleoceanography* 12(4), pp.
852 560–567.
853 Obata A. (2007): Climate carbon cycle model response to freshwater discharge into the North
854 Atlantic. *Journal of Climate* 20(24), pp. 5962-5976.
855 Paillard D., Ghil M. and Treut H. L. (1993): Dissolved organic mater and the glacial-
856 interglacial pCO_2 problem. *Global Biogeochemical Cycles* 7(4), pp. 901-914.
857 Paillard D., Labeyrie L. and Yiou P. (1996): Macintosh program performs time-series
858 analysis. *EOS, transactions American Geophysical Union* 77(39), p. 379.
859 Parrenin F., Barnola J.-M., Beer J., Blunier T., Castellano E., Chappellaz J., Dreyfus G.,
860 Fischer H., Fujita S., Jouzel J., Kawamura K., Lemieux-Dudon B., Loulergue L., Masson-
861 Delmotte V., Narcisi B., Petit J.-R., Raisbeck G., Raynaud D., Ruth U., Schwander J., Severi
862 M., Spahni R., Steffensen J. P., Svensson A., Udisti R., Waelbroeck C. and Wolff E. (2007):
863 The EDC3 chronology for the EPICA Dome C ice core. *Clim. Past* 3(3), pp. 485-497.
864 Pataki D.E., Ehleringer J.R., Flanagan L.B., Yakir D., Bowling D.R., Still C.J., Buchmann N.,
865 Kaplan J.O. and Berry J.A. (2003): The application and interpretation of Keeling plots in

terrestrial carbon cycle research. *Global Biogeochemical Cycles*, 17(1), 1022, DOI: 10.1029/2001GB001850.

Pépin L., Raynaud D., Barnola J.-M. and Loutre M. F. (2001): Hemispheric roles of climate forcings during glacial-interglacial transitions as deduced from the Vostok record and LLN-2D model experiments. *Journal of Geophysical Research* 106, D23, pp. 31885–31892.

Rasmussen S. O., Andersen K. K., Svensson A. M., Steffensen J. P., Vinther B. M., Clausen H. B., Siggaard-Andersen M.-L., Johnsen S. J., Larsen L. B., Dahl-Jensen D., Bigler M., Röthlisberger R., Fischer H., Goto-Azuma K., Hansson M. E. and Ruth U. (2006): A new Greenland ice core chronology for the last glacial termination. *Journal of Geophysical Research* 111, D06102, DOI: 10.1029/2005JD006079.

Rickaby R. E. M., and H. Elderfield (2005): Evidence from the high-latitude North Atlantic for variations in Antarctic Intermediate water flow during the last deglaciation. *Geochemistry Geophysics Geosystems* 6, Q05001, DOI: 10.1029/2004GC000858.

Roethlisberger R., Mulvaney R., Wolff E. W., Hutterli M. A., Bigler M., Sommer S. and Jouzel J. (2002): Dust and sea salt variability in central East Antarctica (Dome C) over the last 45 kyrs and its implications for southern high-latitude climate. *Geophysical Research Letters* 29(20) pp. 24-1, Cite ID 1963, DOI: 10.1029/2002GL015186.

Schmittner A., Brook E. and Ahn J. (2007): Impact of the Ocean's Overturning Circulation on Atmospheric CO_2. *AGU Geophysical Monograph Series* 173, pp. 209-246.

Scholze M., Knorr W. and Heimann M. (2003): Modelling terrestrial vegetation dynamics and carbon cycling for an abrupt climatic change event. *The Holocene* 13(3), pp. 327-333.

Schulz M., Seidov D., Sarnthein M. and Stattegger K. (2001): Modeling ocean-atmosphere carbon budgets during the Last Glacial Maximum - Heinrich 1 Meltwater Event - Bølling transition. *Int. Journ. Earth Sciences* 90, pp. 412-425.

890 Schwander J., Barnola J.-M., Andrié C., Leuenberger M., Ludin A., Raynaud D. and Stauffer
891 B. (1993): The age of the air in the firn and the ice at Summit, Greenland. *Journal of*
892 *Geophysical Research* 98(D2), pp. 2831–2838.
893 Severinghaus J. P., Grachev A. and Battle M. (2001): Thermal fractionation of air in polar firn
894 by seasonal temperature gradients. *Geochemistry, Geophysics, Geosystems* 2(7) 1048, DOI:
895 10.1029/2000GC000146.
896 Sigman D., and E. Boyle (2000): Glacial/interglacial variations in atmospheric carbon
897 dioxide. *Nature* 407(6806), pp. 859-869.
898 Smith H. J., Fischer H., Wahlen M., Mastroianni D. and Deck B. (1999): Dual modes of the
899 carbon cycle since the Last Glacial Maximum. *Nature* 400(6741), pp. 248-250.
900 Spahni R., Schwander J., Flückiger J., Stauffer B., Chappellaz J. and Raynaud D. (2003): The
901 attenuation of fast atmospheric CH_4 variations recorded in polar ice cores. *Geophysical*
902 *Research Letters* 30(11), 1571, DOI: 10.1029/2003GL017093.
903 Spero H. J. and D. W. Lea (2002): The cause of carbon isotope minimum events on glacial
904 terminations. *Science*, 296(5567), pp. 522-525.
905 Stephens B. B., and R. F. Keeling (2000): The influence of Antarctic sea ice on glacial-
906 interglacial CO_2 variations. *Nature*, 404(6774), pp. 171-174.
907 Stott L., J. Southon, A. Timmermann, and A. Koutavas (2009): Radiocarbon age anomaly at
908 intermediate water depth in the Pacific Ocean during the last deglaciation, *Paleoceanography*,
909 24, PA2223, DOI: 10.1029/2008PA001690
910 Toggweiler J. R. (1999): Variation of atmospheric CO_2 by ventilation of the ocean's deepest
911 water. *Paleoceanography* 14(5), pp. 571-588.
912 Toggweiler J. R., Russell J. L. and Carson S. R. (2006): Midlatitude westerlies, atmospheric
913 CO_2, and climate change during the ice ages. *Paleoceanography* 21, PA2005, DOI:
914 10.1029/2005PA001154.

915 Trudinger C. M., Enting L. G., Etheridge D. M., Francey R. J., Levchenko V. A., Steele L. P.,
916 Raynaud D. and Arnaud L. (1997): Modeling air movement and bubble trapping in firn.
917 *Journal of Geophysical Research* 102(D6), pp. 6747–6763.
918 Tschumi J. and Stauffer B. (2000): Reconstructing past atmospheric CO_2 concentration based
919 on ice-core analyses: open questions due to in situ production of CO_2 in the ice. *Journal of*
920 *Glaciology* 46(152), pp. 45-53.
921 Visser K., Thunell R. and Stott L. (2003): Magnitude and timing of temperature change in the
922 Indo-Pacific warm pool during deglaciation. *Nature* 421(6919), pp. 152-155.
923 Watson A. J., and Naveira Garabato A. C. (2006): The role of Southern Ocean mixing and
924 upwelling in glacial-interglacial atmospheric CO_2 change. *Tellus B*, 58(1), pp. 73-87.
925

926 **Figure captions**

927

928 **Figure 1.**

929 CO_2 and $\delta^{13}CO_2$ evolution during the last deglaciation from the EPICA Dome C (EDC) ice
930 core, superimposed with other ice core data: (a) δD of ice in EDC (grey line, [Jouzel et al.,
931 2007]), averaged over 500y (black line, [EPICA, 2006]) (b) $\delta^{18}O$ of NGRIP ice [NGRIP,
932 2004], with a running average over 500y (dark grey line), (c) atmospheric CH_4 mixing ratio
933 (red line and triangles: EDC [Loulergue et al., 2008]; green dots: TD [Brook et al., 2000]), (d)
934 atmospheric CO_2 mixing ratio (red line and dots: EDC [Monnin et al., 2001]; blue line and
935 diamonds: this study; green dots: TD [Smith et al., 1999]) and (e) $\delta^{13}CO_2$ data (blue line and
936 diamonds: this study; green dots: TD [Smith et al., 1999]). When duplicate measurements
937 were performed, the line runs through the mean. The dotted blue lines in (e) correspond to the
938 1σ (0.1 ‰ average) uncertainty envelope. The two blue open diamonds indicate a suspicious
939 result that we discarded in the discussion.

All gas records are plotted versus the Greenland GICC05 age scale. The upper x-axis represents the EDC depth for the gas records. δD is plotted on a chronology combining the CH_4 fit to GICC05 and the EDC3 Δage [EPICA, 2006]. The vertical dotted lines correspond to boundaries between different CO_2 rates of change during the deglaciation, as defined by [Monnin et al., 2001], adapted to the new age scale. The time periods in-between are noted SP-I to SP-IV. YD: Younger Dryas; B/A: Bølling/Allerød; ACR: Antarctica Cold Reversal; H1: Heinrich 1.

Figure 2.

Comparison of atm. $\delta^{13}CO_2$ data with C-cycle related tracers during TI: (a) dust concentration in the EDC core, taken as proxy of the biological pump G-IG patterns in the S. ocean [Lambert et al., 2008]; (b) atmospheric $\delta^{13}CO_2$, from this study; (c) $^{231}Pa/^{230}Th$ in the subtropical North Atlantic, a tracer of North Atlantic Deep Waters formation strength [McManus et al., 2004]; (d) benthic $\delta^{13}C$ in North Atlantic intermediate waters, reflecting the relative contribution between NADW and Antarctic intermediate waters throughout TI in the N. Atlantic basin [Rickaby & Elderfield, 2005]; (e) $\Delta^{14}C$ data of intermediate waters in North Pacific, a proxy for S. Ocean overturning strength [Marchitto et al., 2007]; (f) planktonic $\delta^{13}C$ data from the western tropical Pacific [Stott et al., 2009], also depicting changes in S. Ocean G-IG overturning changes; (g) opal flux data from the Atlantic sector of the S. Ocean, a proxy for S. Ocean upwelling [Anderson et al., 2009]. Atmospheric $\delta^{13}CO_2$ is plotted versus the Greenland GICC05 age scale, while the dust data are presented on the GICC05 ice scale. The oceanic proxies are on their original time scale. Shaded parts represent the cold periods of the North Hemisphere, as deduced from the individual time scales for each proxy.

965 **Figure 3.**

966 Proxy data sets used as BICYCLE input parameterizations. Shadings highlight the definition
967 of sub-periods given in the main text.

968 A: Coral reef terraces as indicator for sea level rise [Fairbanks, 1989].

969 B: NorthGRIP $\delta^{18}O$ as northern high latitude temperature proxy [NGRIP Members, 2004].

970 C: Changes in equatoral SST [Visser et al., 2003] and deep ocean temperature in different
971 oceanic compartments [Labeyrie et al., 1987].

972 D: EDC δD as southern high latitude temperature proxy [Jouzel et al., 2001].

973 E: EDC non-seasalt (nss) dust as proxy of aeolian iron input into the S. Ocean [Roethlisberger
974 et al., 2002].

975 F: Assumed changes in strengths of the main oceanic currents.

976 For B, D and E cases, data show large short term fluctuations; therefore a 500-y running mean
977 is used in the simulations.

978 All ice core records (B, D, E) are plotted versus the GICC05 age scale.

979

980 **Figure 4**

981 Mixing diagram depicting the relationship between atmospheric $\delta^{13}CO_2$ and the inverse of
982 CO_2 (Keeling plot). The new data are shown as open circles with different colors,
983 corresponding to the different sub-periods defined in the main text. BICYCLE model ouput is
984 represented by open black diamonds. Data points used for calculating the regression lines
985 corresponding to the two periods of abrupt CO_2 rise and $\delta^{13}CO_2$ decline are filled with light
986 blue (for the first ^{13}C dip) and dark blue (for the second ^{13}C dip). Filled black diamonds
987 represent model results used for plotting the corresponding regression black lines. The y-
988 intercept values are shown next to the regression lines, together with the number data points.

989 The y-intercepts of the two rapid $\delta^{13}CO_2$ decreases give reasonably consistent values of ~-
990 11‰, comparable with the model results.
991
992 **Figure 5.**
993 Comparison between EDC CO_2 and $\delta^{13}CO_2$ data and box-model simulations.
994 Left panels:
995 Imprint of individual major C-cycle processes on atmospheric (a) CO_2 and (b) $\delta^{13}CO_2$,
996 simulated with the BICYCLE model. All curves express an anomaly ΔpCO_2 and $\Delta\delta^{13}CO_2$
997 versus a reference corresponding to boundary EH conditions. The following processes are
998 shown at this point:
999 (1) S. Ocean mixing; (2) marine productivity; (3) ocean temperature and (4) terrestrial
1000 biosphere.
1001 Right panels:
1002 Superposition of the BICYCLE simulation integrating all individual processes of the left
1003 panels (grey line) with our data (deep blue line and diamonds). The equilibrium-state
1004 BOXKIT model outputs, using similar boundary conditions as BICYCLE for each time
1005 period (red triangles) are also plotted for (c) CO_2 and (d) $\delta^{13}CO_2$. Red squares correspond to
1006 BOXKIT simulations using higher equatorial SST magnitudes. All series are plotted versus
1007 GICC05 age scale.
1008
1009 **Tables**
1010
1011 **Table 1**: Blank tests results of the experimental setup on standard gas, with their 1σ standard
1012 deviation and the number of tests.
1013

Test	CO_2 (ppmv)	$\delta^{13}CO_2$ (‰)	tests number (n)
II	261.1 ± 1.2	-6.4 ± 0.1	5
III	261.4 ± 1.8	-6.7 ± 0.1	14

1014

1015

1016 **Table 2**: Tie-points between the EDC3_gas_a [Loulergue et al., 2007] and GICC05 time
1017 scales [EPICA Community Members, 2006; Andersen et al., 2007; NGRIP Members, 2004]
1018 using the ANALYSERIES software [Paillard et al., 1996]

1019

EDC3_gas-a age (y BP)	GICC05 gas age (y BP)	CH_4 value (ppbv)	event description
7890	8240	590	CH_4 minimum during Holocene
11330	11680	560	CH_4 mid-rise / ending of YD
11920	12330	460	CH_4 YD minimum
12340	12790	540	CH_4 mid decrease / ending of B/A
13070	13600	670	B/A CH_4 peak
14010	14640	570	CH_4 mid-rise / towards B/A
15870	16200	470	CH_4 peak
17790	17800	370	CH_4 drop
19690	19670	350	CH_4 drop
21220	21100	350	CH_4 drop during LGM

1020

1021 Tie-points between TD and GICC05 age scales, using the same software of [Paillard et al.,
1022 1996]. The TD-core was initially plotted versus GISP2 age scale [Brook et al., 2000]. GISP2
1023 is almost synchronous to GICC05; still, for the LGM time-period, GISP2 had to be rescaled:

1024

TD gas age (y BP)	**GICC05 gas age (y BP)**	**CH_4 value (ppbv)**	**event description**
8300	8290	570	CH_4 minimum during Holocene
11690	11660	660	CH_4 peak after YD
11890	11860	430	CH_4 YD minimum
12910	12830	600	CH_4 mid decrease / ending of B/A
13570	13430	670	B/A CH_4 peak
14880	14790	510	Just before the B/A CH_4 rise
16770	16200	500	CH_4 peak before B/A
26470	22810	420	CH_4 peak during LGM

1025

1026

EDC depth (m)

320 350 400 450 500 550 580

IV III II I

e

-6.2 -6.4 -6.6 -6.8 -7 -7.2

$\delta^{13}CO_2$ (‰)

c

800 700 600 500 400

CH_4 (ppbv)

d

280 260 240 220 200 180

CO_2 (ppmv)

b

-36 -38 -40 -42 -44 -46

$\delta^{18}O$ (‰)

a

-380 -400 -420 -440

δD(‰)

YD B/A ACR H1

8 10 12 14 16 18 20 22 24 26

Age (ky BP)

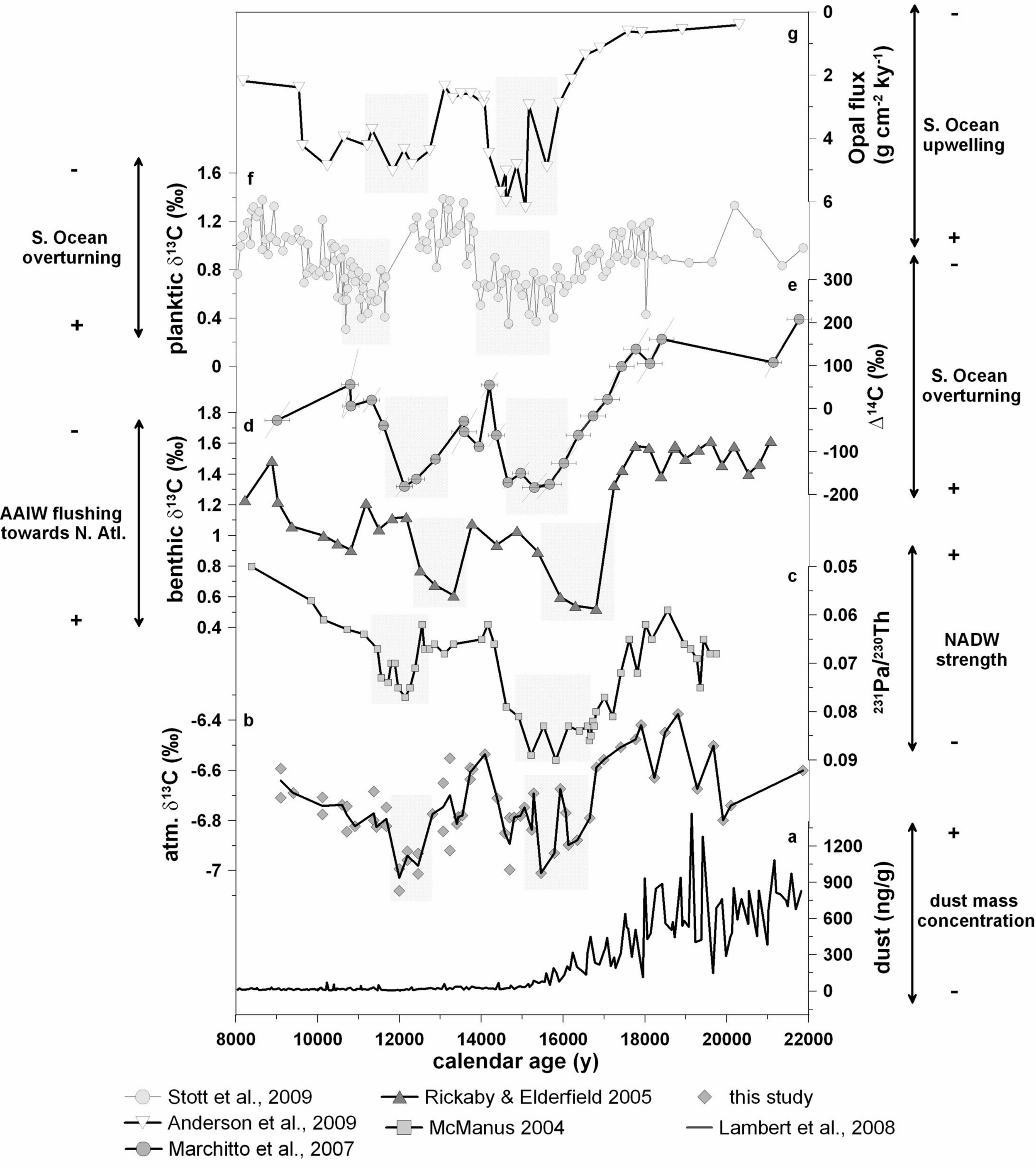
g
f
e
d
c
b
a
planktic δ13C (‰)
benthic δ13C (‰)
atm. δ13C (‰)
Opal flux (g cm-2 ky-1)
Δ14C (‰)
231Pa/230Th
dust (ng/g)
S. Ocean overturning
S. Ocean upwelling
AAIW flushing towards N. Atl.
NADW strength
dust mass concentration
calendar age (y)
Stott et al., 2009
Anderson et al., 2009
Marchitto et al., 2007
Rickaby & Elderfield 2005
McManus 2004
this study
Lambert et al., 2008

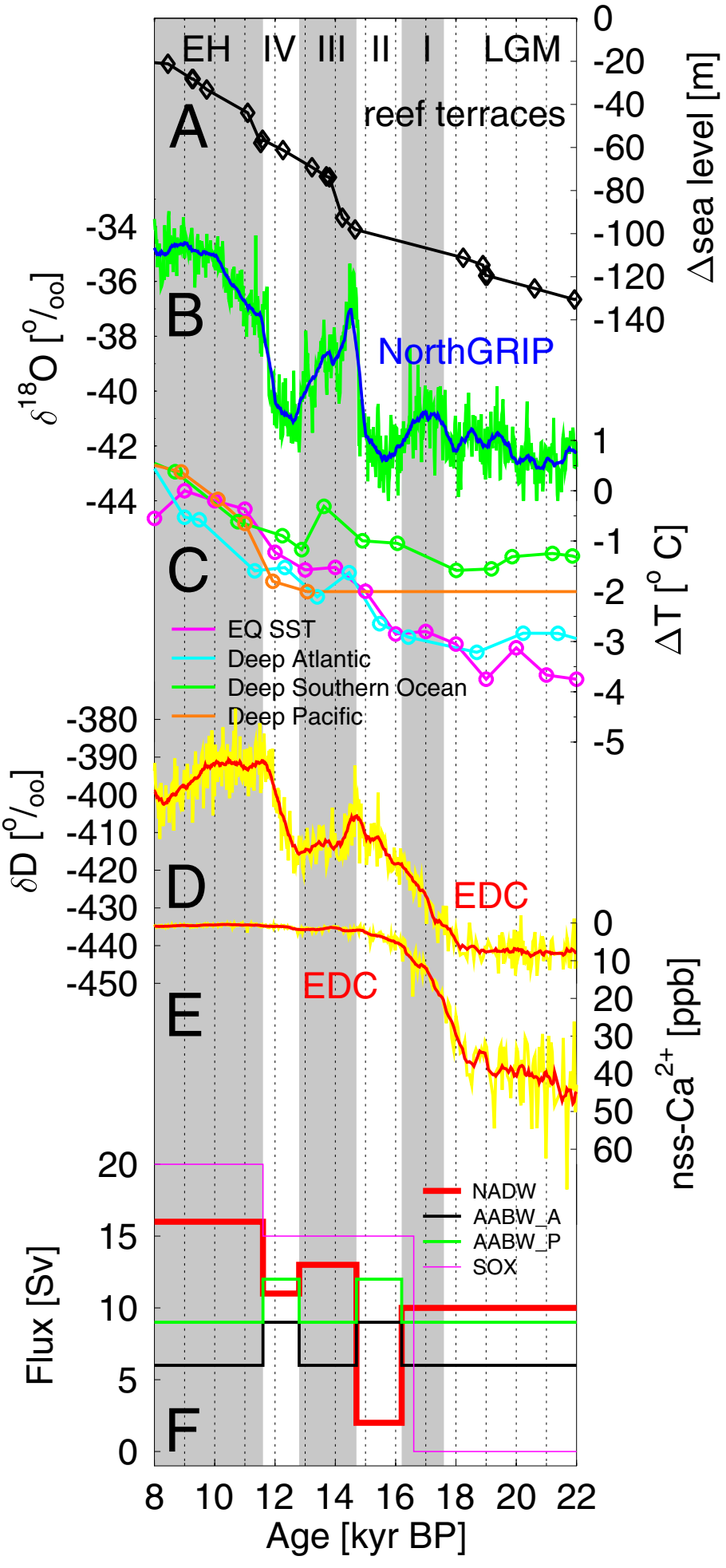
EH
IV
III
II
I
LGM
A
reef terraces
Δsea level [m]
0
-20
-40
-60
-80
-100
-120
-140
B
NorthGRIP
δ18O [o/oo]
-34
-36
-38
-40
-42
-44
C
EQ SST
Deep Atlantic
Deep Southern Ocean
Deep Pacific
ΔT [o C]
1
0
-1
-2
-3
-4
-5
δD [o/oo]
-380
-390
-400
-410
-420
-430
-440
-450
D
EDC
E
EDC
nss-Ca2+ [ppb]
0
10
20
30
40
50
60
Flux [Sv]
20
15
10
5
0
F
NADW
AABW_A
AABW_P
SOX
8
10
12
14
16
18
20
22
Age [kyr BP]

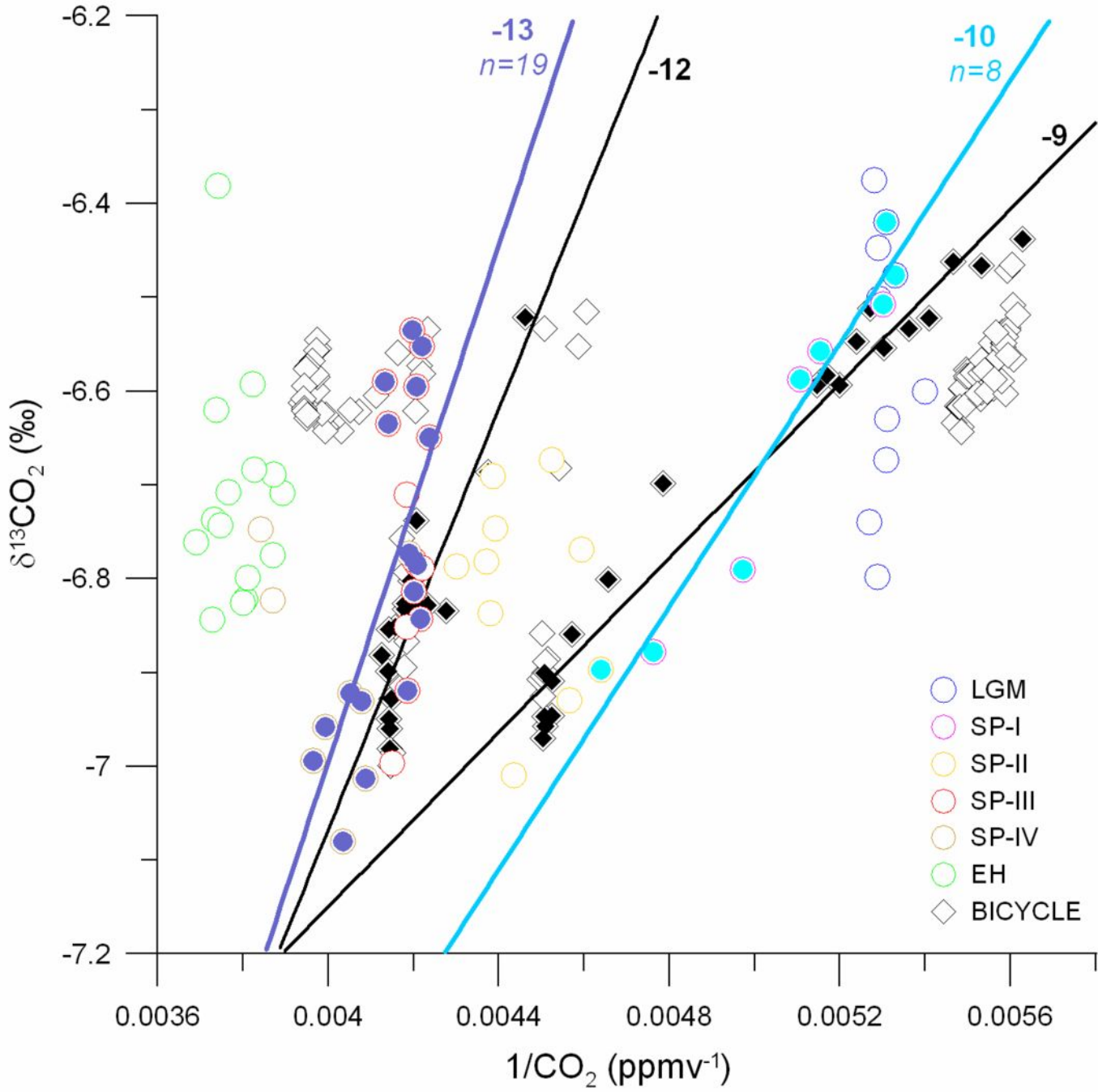
-13
n=19
-12
-10
n=8
-9
LGM
SP-I
SP-II
SP-III
SP-IV
EH
BICYCLE
-6.2
-6.4
-6.6
-6.8
-7
-7.2
δ13CO2 (‰)
0.0036
0.004
0.0044
0.0048
0.0052
0.0056
1/CO2 (ppmv-1)

b

IV III II I

$\Delta\delta^{13}C$ (‰)

1 2 3 4

a

4

ΔpCO_2 (μatm)

3 2 1

S. Ocean mixing
Marine productivity
Ocean Temperature
Terrestrial biosphere

Age (ky BP)

d

IV III II I

$\delta^{13}C$ (‰)

c

pCO_2 (ppmv)

EDC - points
EDC - mean line
BICYCLE
BOXKIT as BICYCLE conditions
BOXKIT *SP-III* SSTs-change

Age (ky BP)

Supporting non-print material

Keeling plot as a function of each sub-period

We provide a Keeling plot where our data are distinguished as a function of each sub-period (open circles and continuous lines, Fig. S1). We find similar regressions for each sub-period between our data and Smith et al., 1999 data (crosses and dotted lines, Fig. S1). The *y*-intercepts are of little use in the case of SP-II, SP-III and SP-IV, due to the very large slope. This highlights again the limit of Keeling plots when used in such context.

BICYCLE model updates

The overall model configuration is seen in fig. S2a, while fig. S2b illustrates in detail the oceanic boxes interactions. Here we use the model version, where terrestrial net primary productivity is more influenced by climate (notably temperature) change than by CO_2 fertilization. This version is labeled "TB2" in former applications [Köhler & Fischer, 2004] (from now on called "GBC2005-version").

Model outputs are given in atmospheric partial pressure (pCO_2) in µatm units, which, only in dry air and at standard pressure conditions are identical to ice core nomenclature (ppmv); we assume equality between the two, neglecting a relatively constant offset between both quantities of a few ppmv.

Here an update of the "GBC2005" version is presented, named ("GBC2009"). The modifications mainly concern oceanic processes

(a) Carbonate compensation is represented by a relaxation function, which brings deep ocean carbonate ion concentration, CO_3^{2-}, back to initial values after every perturbation. This relaxation operates with a time delay (e-folding time) of τ = 1.5 ky to account for the relatively slow processes in the sediments. This value of τ was chosen based on reconstructed

deep ocean carbonate ion dynamics [Marchitto et al., 2005]. Details of the approach are described in [Köhler & Fischer, 2006].

(b) In terms of ocean circulation changes, we assumed a reduction of NADW by 8 Sv during H1, instead of the complete shutdown initially proposed [Köhler et al., 2005]. We also changed AABW in antiphase with NH deep waters, in order to better represent the bipolar seesaw in the simulations. Furthermore, 30% of upwelling fluxes in the S. Ocean are directly redistributed to the Atlantic intermediate waters.

Fig. S3 illustrates the new GBC2009 integrated result against our data and the older GBC2005 model simulations, (a) for CO_2 and (b) for $\delta^{13}CO_2$. This new GBC2009 version of BICYCLE leads to the following improvements:

1. LGM and EH boundary values are more consistent with our data
2. The timing and trend of the early deglaciation are better reconstructed, due to updated runs using the most recent age scale GICC05. Still, inconsistencies exist for the last two SPs of TI, as for the case of TB2; the model trends lead the data.
3. The magnitudes of both CO_2 and $\delta^{13}CO_2$ changes throughout the different SPs are more consistent with our data.

The largest discrepancy between our data and BICYCLE new version lies in the EH. It could be explained by inadequate ocean circulation parameterisation: for instance AABW gets stable in BICYCLE simulations at the end of YD, whereas it should have been enhanced at that time, as for NADW.

Fig. S4 finally shows the contribution of the three less important forcing factors towards the atmospheric CO_2 and $\delta^{13}CO_2$, and are already been commented in the main text.

Figure captions

Figure S1

Mixing diagram depicting the relationship between atmospheric $\delta^{13}CO_2$ and the inverse of CO_2 (Keeling plot). The new data are shown as open circles with different colors, corresponding to the different sub-periods defined in the main text. The data from Smith et al., 1999 are provided as crosses with a color coding similar to our data, for each sub-period they belong to. Regression lines for both datasets are plotted as well for each sub-period (continuous lines and dashed lines respectively).

Figure S2

Sketch of the "Box model of the Isotopic Carbon cYCLE" (BICYCLE).

(a) Overall model setup.

Compartments in the terrestrial biosphere distinguish different primary production schemes for grasses (C3, C4), non woody (NW) and woody (W) biomass of tree, detritus (D) and fast and slow (FS, SS) decomposing soils.

(b) Close-up on the definition of ocean boxes and the circulation scheme, fluxes quantified for the pre-industrial period (PRE).

Fluxes are given in Sverdrup ($1Sv = 10^6\ m^3/s$)

Figure S3

Comparison of both BICYCLE model versions (black lines) to our dataset (blue diamonds). The dotted line corresponds to the initial BICYCLE (GBC2005) simulation throughout TI, as described in the main manuscript. The straight line corresponds to our modified BICYCLE

GBC2009-configuration. (a) gives the result on CO_2 and (b) for $\delta^{13}CO_2$. Both plots are on the GICC05 age scale.

Figure S4

Impact of less important forcing factors on the atmospheric (a) CO_2 and (b) $\delta^{13}CO_2$ signal: (5) sea level rise; (6) sea ice retreat and (7) Northern (NADW) and Southern (AABW)- sourced deep water fluxes changes, throughout TI. All curves express an anomaly ΔpCO_2 and $\Delta\delta^{13}CO_2$ versus a reference representing the boundary EH conditions.

Figures

Figure S1

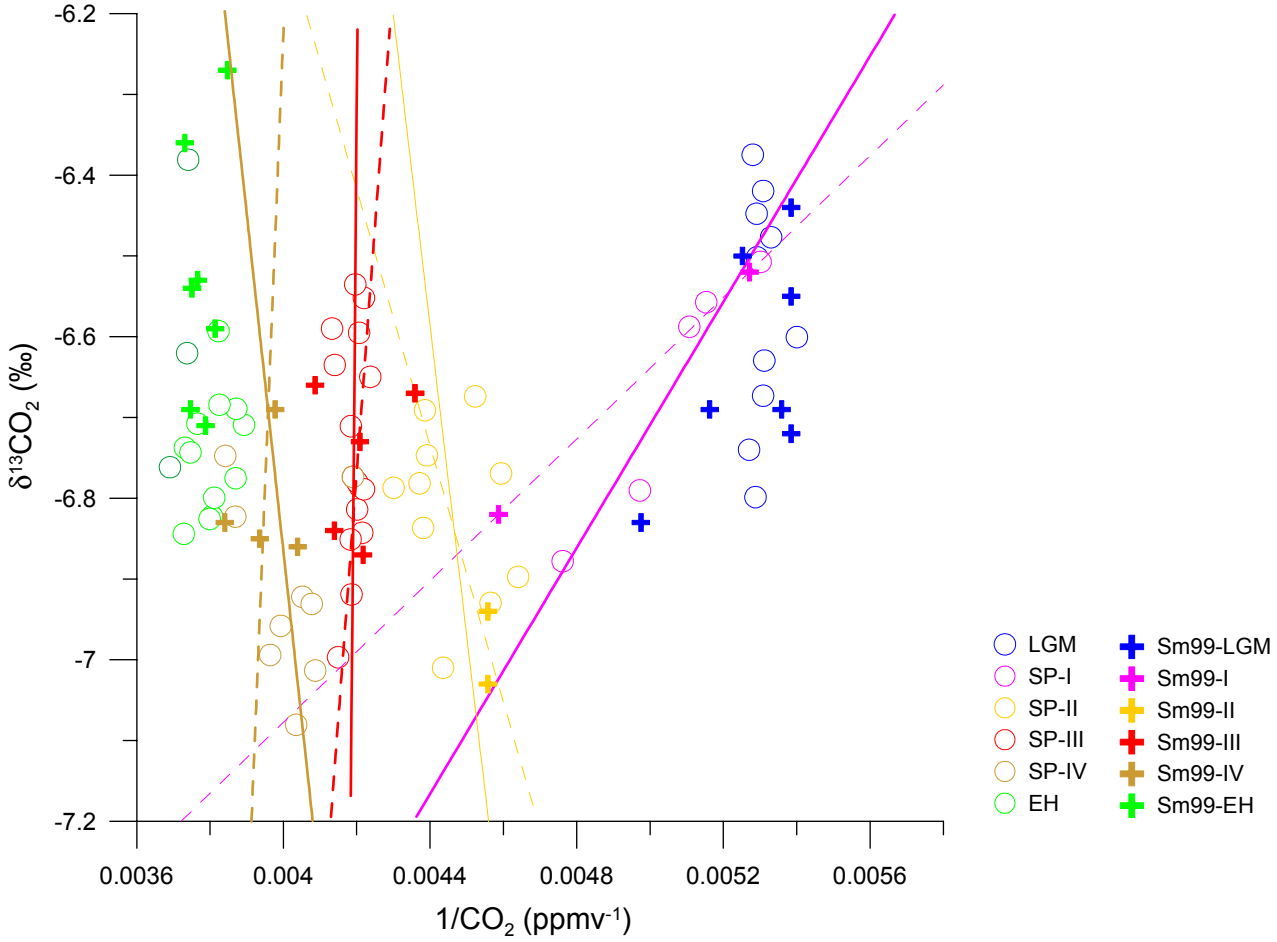
-6.2
-6.4
-6.6
-6.8
-7
-7.2
δ13CO2 (‰)
0.0036
0.004
0.0044
0.0048
0.0052
0.0056
1/CO2 (ppmv-1)
LGM
SP-I
SP-II
SP-III
SP-IV
EH
Sm99-LGM
Sm99-I
Sm99-II
Sm99-III
Sm99-IV
Sm99-EH

Figure S2

(a)

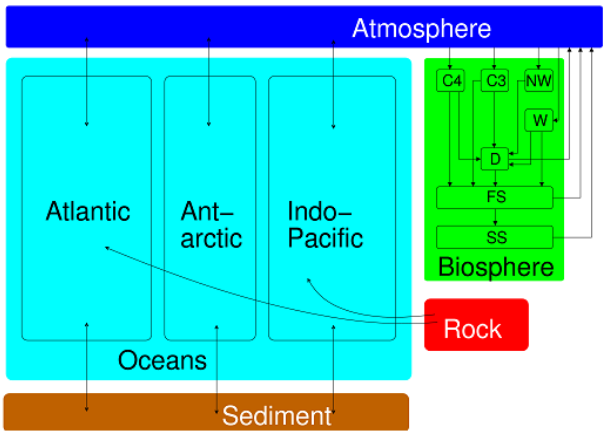
Atmosphere
Atlantic
Ant–
arctic
Indo–
Pacific
Oceans
Sediment
C4
C3
NW
W
D
FS
SS
Biosphere
Rock

(b)

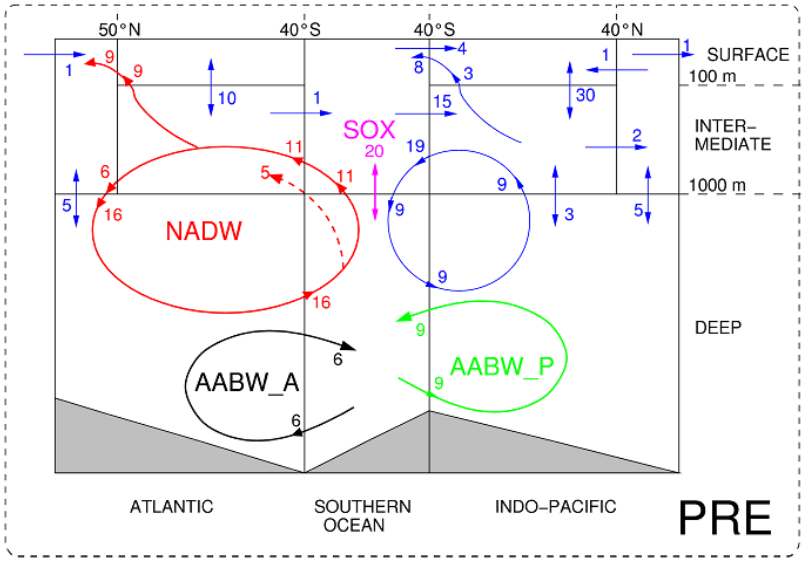
50°N
40°S
40°S
40°N
SURFACE
100 m
INTER–
MEDIATE
1000 m
DEEP
SOX
20
NADW
AABW_A
AABW_P
ATLANTIC
SOUTHERN
OCEAN
INDO–PACIFIC
PRE

Figure S3

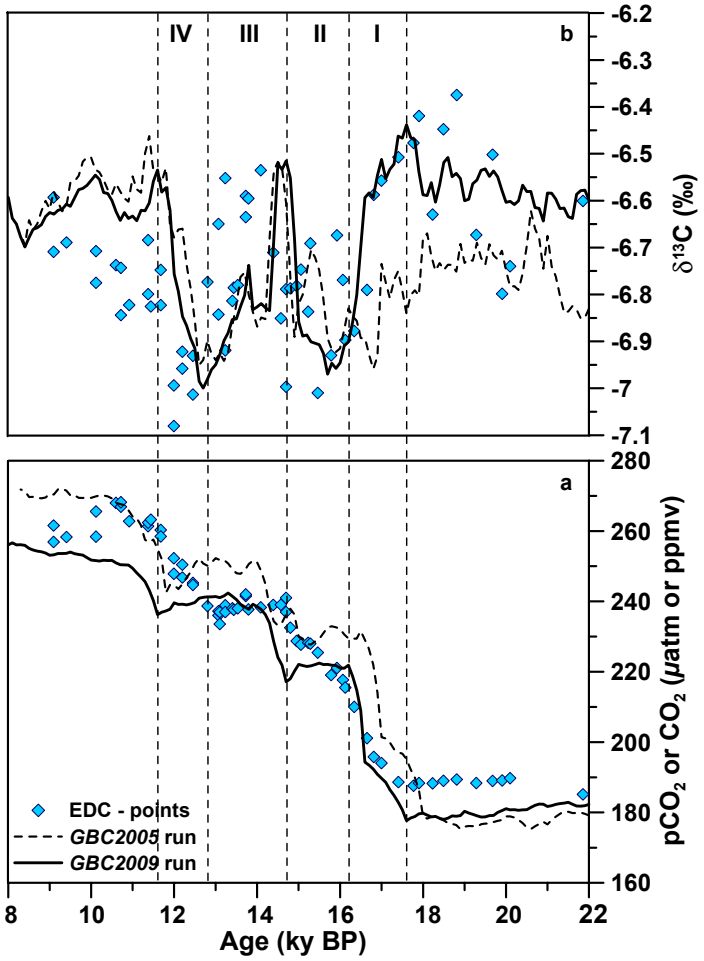
IV
III
II
I
b
a
-6.2
-6.3
-6.4
-6.5
-6.6
-6.7
-6.8
-6.9
-7
-7.1
δ13C (‰)
280
260
240
220
200
180
160
pCO2 or CO2 (µatm or ppmv)
EDC - points
GBC2005 run
GBC2009 run
8
10
12
14
16
18
20
22
Age (ky BP)

Figure S4

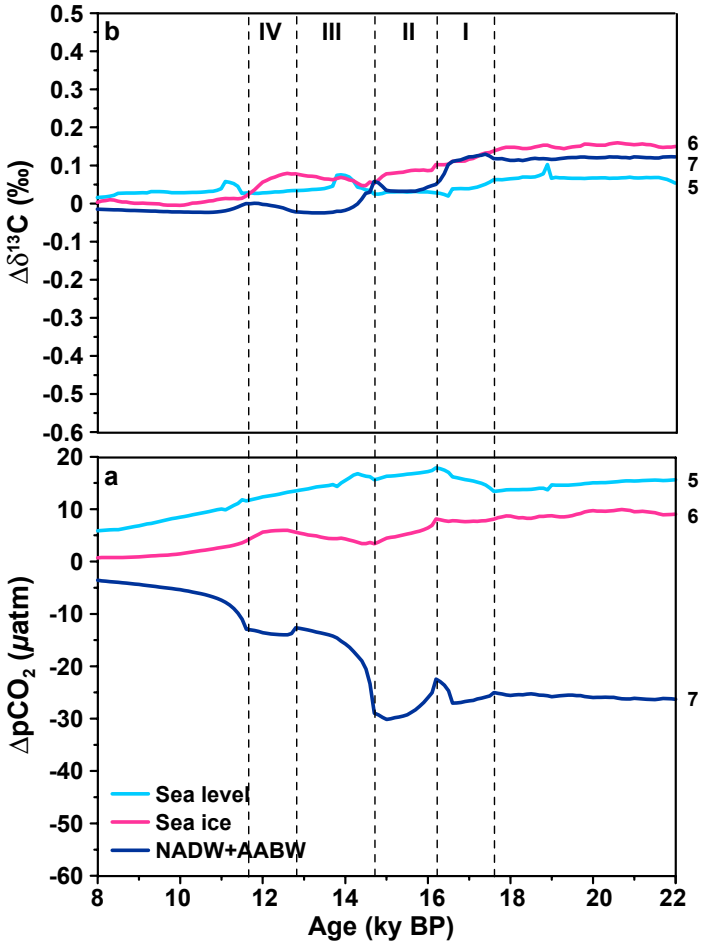

Supplementary References

Köhler P. and Fischer H. (2004): Simulating changes in the terrestrial biosphere during the last glacial/interglacial transition. *Global and Planetary Change* **43(1-2)**, pp. 33-55.

Köhler P., Fischer H., Munhoven G. and Zeebe R. E. (2005): Quantitative interpretation of atmospheric carbon records over the last glacial termination. *Global Biogeochemical Cycles* **19**, GB4020, DOI: 10.1029/2004GB002345.

Köhler P. and Fischer H. (2006): Simulating low frequency changes in atmospheric CO_2 during the last 740,000 years. *Climate of the Past* **2(2)**, pp. 57-78.

Marchitto T. M., Lynch-Stieglitz J. and Hemming S. R. (2005): Deep Pacific $CaCO_3$ compensation and glacial–interglacial atmospheric CO_2. *Earth and Planetary Science Letters* **231(3-4)**, pp. 317-336.

Smith H. J., Fischer H., Wahlen M., Mastroianni D. and Deck B. (1999): Dual modes of the carbon cycle since the Last Glacial Maximum. *Nature* **400(6741)**, pp. 248-250.